

# The 2015-2016 Earthquake Sequence in Cushing, Oklahoma driven by Coulomb Stress Changes and Fluid Diffusions

Qingjun Meng<sup>1</sup>, Sidao Ni<sup>2</sup>, and Zhigang Peng<sup>3</sup>

<sup>1</sup>Department of Geology and Geophysics, Texas A&M University

<sup>2</sup>State Key Laboratory of Geodesy and Earth's Dynamics, Institute of Geodesy and Geophysics, Chinese Academy of Sciences

<sup>3</sup>School of Earth and Atmospheric Sciences, Georgia Institute of Technology

November 24, 2022

## Abstract

An M5 earthquake occurred on November 7th, 2016, near the city of Cushing in Oklahoma, the largest crude oil storage site in the USA, after nearby disposal wells had been shut-in responding to three M4+ earthquakes in 2015. In this study, we investigated the rupture process of these M4+ events with finite fault model (FFM) inversions and computed Coulomb stress changes during this Cushing sequence. We found that the rupture processes of the four M4+ earthquakes are very complex, and they appeared to trigger one another, as evidenced by the inverted finite fault slip distribution and the calculated Coulomb stress change after each event. The foreshocks of the first M4 earthquake are probably triggered by Coulomb stress changes from previous earthquakes during 2014 and 2015 on unmapped faults several kilometers to the south. Fluid diffusion likely drives the bilateral seismic migration of the Cushing earthquake sequence after the foreshocks were triggered. In addition, fluid injection from the northwest of Cushing fault might have gradually increased the pore pressure on the Cushing fault, making the shallow part of the fault critically stressed.

1     **The 2015-2016 Earthquake Sequence in Cushing, Oklahoma driven by**  
2                     **Coulomb Stress Changes and Fluid Diffusions**

3

4                             Qingjun Meng <sup>1</sup>, Sidao Ni <sup>2</sup>, Zhigang Peng <sup>3,\*</sup>

5<sup>1</sup> Department of Geology and Geophysics, Texas A&M University, College Station, TX, USA

6   (qimeng@tamu.edu)

7<sup>2</sup> State Key Laboratory of Geodesy and Earth's Dynamics, Institute of Geodesy and Geophysics,

8   Chinese Academy of Sciences, Wuhan, China (sdni@apm.ac.cn)

9<sup>3</sup> School of Earth and Atmospheric Sciences, Georgia Institute of Technology, Atlanta, GA, USA

10   (zpeng@gatech.edu)

11 Corresponding author: Zhigang Peng (zpeng@gatech.edu)

12

13 **Key Points:**

14 Slip distributions of the Cushing earthquake sequence are complex and complement with each

15 other

16 Coulomb stress changes likely explain the space-time evolution of the Cushing earthquake

17 sequence

18 Fluid diffusion also plays an important role in driving foreshock and aftershock migration

19

**21Abstract**

22An M5 earthquake occurred on November 7th, 2016, near the city of Cushing in Oklahoma, the  
23largest crude oil storage site in the USA, after nearby disposal wells had been shut-in responding  
24to three M4+ earthquakes in 2015. In this study, we investigated the rupture process of these M4+  
25events with finite fault model (FFM) inversions and computed Coulomb stress changes during  
26this Cushing sequence. We found that the rupture processes of the four M4+ earthquakes are very  
27complex, and they appeared to trigger one another, as evidenced by the inverted finite fault slip  
28distribution and the calculated Coulomb stress change after each event. The foreshocks of the  
29first M4 earthquake are probably triggered by Coulomb stress changes from previous  
30earthquakes during 2014 and 2015 on unmapped faults several kilometers to the south. Fluid  
31diffusion likely drives the bilateral seismic migration of the Cushing earthquake sequence after  
32the foreshocks were triggered. In addition, fluid injection from the northwest of Cushing fault  
33might have gradually increased the pore pressure on the Cushing fault, making the shallow part  
34of the fault critically stressed.

35

**36Plain Language Summary**

37We studied the rupture process of four M4+ earthquakes and their foreshocks/aftershocks  
38evolution process of the Cushing sequence, which occurred near the Cushing oil storage facilities  
39and water disposal wells during 2015 and 2016. We found that the hypocenters of the four M4+  
40earthquakes occurred closely and their seismic slip patches complement each other in space on  
41the unmapped Cushing fault. For the M4+ events, the stress status change caused by former

42events contribute to triggering later event, implying a cascading trigger effect. Years before the  
43Cushing sequence, the seismicity gradually migrated from several faults on south of Cushing  
44fault until the foreshock sequence of Cushing sequence started, indicating foreshocks triggering  
45effect. Both the foreshock triggering and the M4+ events triggering might be closely related with  
46the water injection activity on northwest of Cushing city, because it might have increased the  
47fluid pressure on the Cushing fault, making it a critically stressed fault susceptible for static  
48stress triggering. The seismic bilateral expansions during the Cushing sequence also suggest a  
49role by fluid diffusion. The seismic activity may be a composite product of both injection and  
50tectonic stress transfer, that seismicity may start from areas far from the injection zone.

51

52

### 531. Introduction

54 Seismicity increased substantially in central United States beginning in 2008 (Ellsworth, 2013),  
55 and earthquakes in Oklahoma are the primary contributor of this surge (Keranen et al., 2014),  
56 with four  $M$  5+ earthquakes occurred since 2011. Recent studies have shown that the sharp  
57 increase of seismicity and frequent occurrence of moderate-size events in Oklahoma are most  
58 likely linked with water disposal activity and hydraulic fracturing (e.g., Keranen et al., 2013;  
59 Yeck et al., 2017; Chen et al., 2017; Skoumal et al., 2019).

60 Several mechanisms have been proposed to explain the occurrence of induced earthquakes,  
61 including pore pressure increase resulted from fluid diffusion (Shapiro et al., 1997; Keranen et  
62 al., 2013; Chen et al., 2017), aseismic slip (Wei *et al.*, 2015), foreshock-induced Coulomb stress  
63 changes (Sumy *et al.*, 2014) and poro-elastically induced Coulomb stress changes (Segall and  
64 Lu, 2015; Goebel et al., 2017). In addition, recent studies attempted to examine other factors that  
65 govern locations and occurrence rates of induced earthquakes, such as injection volume and rates  
66 (Weingarten et al., 2015), injection depth to crystalline basement (Hincks et al., 2018), and  
67 competencies of rocks inferred from seismic tomography (Pei et al., 2018). However, it is still  
68 not clear which mechanisms or factors play the most important role in determining rate and  
69 maximum size of induced earthquakes (McGarr, 2017; Chen et al., 2018).

70 Most of these studies focus on examining seismicity and injection operations for the entire  
71 Oklahoma state or other regions. Only a few recent studies investigated an individual earthquake  
72 sequence or a small area in details (e.g., Goebel et al., 2017; Chen et al., 2018; Wu et al., 2019).  
73 As different faults might respond to fluid injection distinctively, it would be helpful to examine  
74 individual earthquake sequences to better understand the evolution of seismicity and mainshock  
75 source parameters, as well as the relationship with industrial water injection operation. These

76 results could be used, together with other recent studies, to provide useful information to  
77 operators and regulators in wastewater disposal regions to reduce potential impacts from induced  
78 earthquakes.

79 The M5 Cushing earthquake (November 7<sup>th</sup>, 2016, 01:44:24.500 UTC) is the latest *M* 5 event  
80 in Oklahoma (Figure 1). Similar to previous *M* 5 earthquakes in Oklahoma, it ruptured a  
81 previously unmapped fault (Yeck et al., 2017) about one mile to the west of Cushing city (Figure  
82 1b). Cushing is a strategically important location with numerous intersecting pipelines and  
83 strategic storage facilities for crude oil in USA. Thus, the potential risk of damaging earthquakes  
84 in this region is much larger than in other regions in Oklahoma. While the M5 Cushing  
85 mainshock did not produce any damages to those storage facilities, some structural damages  
86 were found within the city (Taylor et al., 2017).

87 In October 2014, two M4+ earthquakes occurred along another unmapped fault just south of  
88 Cushing city (McNamara et al., 2015), raising the possibility of a large damaging earthquake  
89 along the Wilzetta-Whitetail fault zone further south of Cushing. One year before the 2016  
90 Cushing *M* 5 earthquake, three *M* 4+ events occurred at nearly the same fault west of Cushing  
91 city (*M<sub>w</sub>* 4.1, 09/18/2015 12:35:16.600 UTC; *M<sub>w</sub>* 4.0, 09/25/2015 01:16:37.700 UTC; *M<sub>w</sub>*  
92 4.3, 10/10/2015 22:03:05.300 UTC). After these *M* 4+ events, Oklahoma Corporation  
93 Commission (OCC) required that injection wells within 3 miles from the earthquakes be shut in,  
94 and volume injected for wells within 6 miles should be reduced by 25 percent and wells from 6  
95 to 10 miles may maintain the injection levels unincreased (OCC, 2015). However, a significant  
96 amount of waste water was then injected into a shallower formation (OCC). In November 2016,  
97 the *M* 5 event occurred nearly at the same locations of three *M* 4+ events.

98 Previous studies on  $M$  5+ events in Oklahoma mostly involve teleseismic, InSAR or regional  
99 seismic data to invert for the slip models (Sun et al., 2014; Grandin et al., 2017). The Cushing  
100 earthquake sequence (three  $M$  4+ and one  $M$  5 event) is relatively small in magnitude, with the  
101 largest mainshock only about  $M$  5. Hence, teleseismic and InSAR data do not provide the highest  
102 resolution to reveal detailed rupture processes. Recently, based on local broadband recordings,  
103 Wu et al. (2019) utilized a time domain empirical Green's function (EGF) deconvolution method  
104 to retrieve relative source time functions (RSTFs) of the 2015  $M$  4.0 Guthrie earthquake, and  
105 found four sub-events propagating unilaterally to the southwest. Their study highlighted the  
106 importance of local waveform recordings for high-resolution source imaging of moderate-size  
107 events.

108 For the 2015-2016 Cushing sequence, several nearby seismic stations (with both broadband  
109 and strong motion sensors) are available, including three seismometers within 5 km and the  
110 closest station less than 2 km from the 2016  $M$  5 mainshock, providing an excellent opportunity  
111 to reveal fine details of their rupture processes. Combining with precise microseismicity  
112 relocation results and comparing with the water injection data, we can better understand the  
113 spatio-temporal evolution and triggering behavior of this earthquake sequence.

#### 1142. Spatio-Temporal Evolutions of Seismicity

115 Based on catalogs and phase arrivals from National Earthquake Information Center (NEIC) and  
116 Oklahoma Geological Survey (OGS), Schoenball and Ellsworth (2017a) used HYPOINVERSE-  
117 2000 (Klein, 2014) and hypoDD packages (Waldhauser and Ellsworth, 2000) to relocate  
118 earthquakes in Oklahoma and southern Kansas from May 2013 to November 2016 (Figure 1a-d).  
119 From their relocation result (Figure 1), the 2015-2016 Cushing seismic sequence occurred along  
120 a narrow zone along profile AA' striking  $60^\circ$  clockwise from north, with a nearly vertical fault

121 geometry (hereafter termed the Cushing Fault). This is consistent with the right-lateral strike-slip  
122 focal mechanisms with steep dip angles (Figure 1b and Table 1) from our point-source focal  
123 mechanism inversion results for four events in this sequence (next section). From the relocation  
124 result along profile AA', we found that four *M*4-5 events and their aftershocks occurred at  
125 shallow depth between 2 to 5 km.

126       Next we examined the seismicity pattern in a longer time window (2013-2020). Because  
127 the relocated catalog of Schoenball and Ellsworth (2017a) is between 2013 and 2016, we used  
128 both the relocated (Figure 2) and the standard (Figure S1) OGS catalogs (Walter et al., 2019). In  
129 addition, we compared with a relocated catalog (Figure S2) based on template matching  
130 (Skoumal et al., 2019). Generally, the seismic evolution history near Cushing city could be  
131 summarized by four main stages: I, II, III and IV. In stage I, the seismicity rate was low in 2013  
132 but surged since 2014, concentrating along a short WNW unmapped fault (CC' in Figure 2) on  
133 the south of the Cushing fault (AA' in Figure 2a). The increased seismicity includes two left-  
134 lateral strike slip *M* 4 earthquakes on October 2014 (Figure 2a), implying a left-lateral strike-slip  
135 nature of fault CC' (McNamara et al., 2015). In stage II, between October 2014 to September 18,  
136 2015, a seismic swarm began to concentrate along a ~60 degree striking short fault (marked as  
137 DD' in Figure 2b) to the northwest of the two *M*4 earthquakes. By checking the first motions of  
138 four *M*>3 earthquakes within this warm, it seems that all of them are consistent with right-lateral  
139 strike slip focal mechanisms (Figure S3) and the largest event is of magnitude 3.4 on 09/01/2015.

140       At the end of stage II (09/15/2015), three days before the first *M* 4.1 earthquake on  
141 09/18/2015, seismicity started occurring on the western part of the ENE-striking Cushing fault  
142 (AA' in Figure 2b), followed by three *M* 4+ earthquakes together with their aftershocks along  
143 this right-lateral fault (Figure 2c) a few days later in stage III. The seismicity started at around 3

144km along the AA' projection starting at 09/15/2015 and showed bi-lateral expansion along both  
145directions (Figure 2h). Such expansion is also clear in the original OGS catalog (Figure S1) and  
146the template-matching catalog (Figure S2). Because the seismic activity increased steadily  
147without a mainshock, this sequence can be classified as earthquake swarms (e.g., Mogi, 1990).  
148For the sake of discussion later, we also termed the seismicity before the first M 4.1 event on  
14909/18/2015 as foreshocks. In stage III, after the three M 4+ earthquakes occurred along fault  
150AA', many earthquakes occurred surrounding the Cushing city. Earthquakes started to occur at  
151the eastern end of fault CC' from March to May in 2016 and seismicity started to occur to the  
152north of fault AA' from June to November 2016. In stage IV, following the M 5 event on Nov. 7,  
1532016, nearly all seismicity concentrated along the fault AA' for about 9 kms. The seismic activity  
154on adjacent faults was suppressed since then and the Cushing fault AA' became dominant  
155without significant seismic activity around Cushing area up to 2020 (Figure S1).

### 1563. Path Calibration for Source Inversion

157 Because M4+ events are relatively small, detailed analysis of their rupture process requires  
158modeling of high-frequency seismic waveforms. To ensure that propagation effects are properly  
159modeled at high frequencies, we refined the 1D velocity structure and performed path calibration  
160using four M3+ reference events (Table S1) located along the ruptured fault (Figure 1c-d). For  
161these reference M3+ events, their corner frequencies are higher and source time functions are  
162relatively simpler than the targeted M4-5 events, which could be approximated as point sources.  
163In addition, the four reference events occurred after Nov. 9, 2016, when two close-by seismic  
164stations (OK052 and OK053) were deployed, thus providing valuable data for reliable waveform  
165modeling. Together with other nearby stations (Figure 1), we used hypo2000 method (Klein,

1662014) to gain more precise relocation for these reference events, which improve the path  
167calibration by minimizing the location uncertainty.

168 To obtain a refined velocity structure (Figure 3), we first fixed the basement depth at about  
1692.0 km, which was referred from Keranen et al. (2013) and based on the completion depths of  
170nearby injection wells. We grid searched for an optimal  $V_p$  of the top rock layer and the optimal  
171depth of  $V_p$  equals to 4.0 km/s,  $D_{vp4}$  (Wei et al, 2015). An empirical relationship of  $V_s = (V_p -$   
1721.36)/1.16 was used to estimate  $V_s$  from  $V_p$  within each layer (Brocher, 2005). In addition,  
173considering the effects of unconsolidated sediments in the near surface, a thin (8 m thick) low-  
174velocity layer was added as the top layer, with  $V_p= 1.7$  km/s and  $V_s=0.3$  km/s (Taylor et al.,  
1752017). Within each tested velocity model, we calculated synthetic waveforms of four reference  
176events based on Green's functions computed with a frequency-wavenumber integral algorithm  
177(Zhu and Rivera, 2002) and a uniform focal mechanism of strike/dip/rake of  $60^\circ/90^\circ/0^\circ$ . These  
178numbers are based on the focal mechanisms of the  $M4-5$  earthquakes (Table 1) and the spatial  
179distribution of their aftershocks (Figure 1). To avoid the influence of depth uncertainty from  
180reference events, the focal depth was slightly adjusted around the relocated depth to achieve the  
181best match between the observation and synthetics. Using the optimal refined velocity model  
182VM3 (Table S2), the average correlation-coefficient (CC) between the observed three-component  
183waveforms and the synthetics reaches to the highest value of about 0.54 (Figure S4). In  
184comparison, The Keranen et al. (2013) model VM2 yields an average CC of about 0.38, and the  
185Crust2.0 model (Bassin *et al.*, 2000) VM1 results in an average CC lower than 0.1.

#### 1864. Finite Fault Model and Stress Drop Estimate

187From the raw seismic waveforms, the  $M 5$  mainshock appeared to have two sub-events, and the  
188differential S wave arrival times for two sub-events can be seen clearly on four close seismic

189stations (Figure 4b). By matching the observed and synthetic S waves arrival time difference, we  
190grid-searched the initiation point and origin time of the second sub-event (Figure 4a). Although  
191the depth constraint is relatively poor compared with the horizontal constraint, the second sub-  
192event is found to initiate about 3 km to the north of the first sub-event along the fault, and about  
1931 s later after the first sub-event. This suggests a rupture speed of at least 3 km/s for the M 5  
194mainshock. From the raw seismic data of three M4+ events (Figure 4c), we found that the S  
195waves are also very complex, not as simple and clean as the reference events (Figure S4). This  
196implies that all events in Cushing earthquake sequence involve complicated rupture processes,  
197which could be revealed from the finite fault inversion results below.

198 With the optimal velocity structure, we inverted for the rupture process of M4-5 Cushing  
199earthquakes and calculated their stress drops. We used three-component waveform data from  
200seismic stations within epicentral distance of 15 km, and band-pass filtered velocity waveforms  
201from 0.2 to 3 Hz. Rupture initiation points (i.e., hypocenters) are based on the relocated catalog  
202(Schoenball and Ellsworth, 2017a) and the geometries of fault models are based on focal  
203mechanisms inverted by the Cut and Pasted (CAP) method (Zhu et al., 2013). Then we  
204performed an inversion of finite fault model (FFM) for each event (Hartzell and Heaton, 1983;  
205Yue and Lay, 2013), with the fault model consisting of 77 grids with each cell size of 0.5×0.5  
206km, and the total fault dimensions of 6.5×6.5 km. The source time function (STF) of each grid is  
207parameterized as 6 symmetric triangles of 0.15 s rise time with an offset of 0.15 s each. During  
208the FFM inversion process, the rupture speed for the M 5 mainshock is set at 3 km/s (as inferred  
209from the direct waveform observation in Figure 4a). The rupture speed for three M 4+ events is  
210set as 2.5 km/s, which is about 75% of S wave velocity and could fit the observed waves well.  
211The smoothing factors are set as  $3.5 \times 10^{-5}$ , after comparing the waveforms fitting misfit under a

212series of smoothing factor values (Figure S5) and examining the check-board recovery result  
213(Figure S6).

214 The inverted slip models, waveform fittings and STF's for the four earthquakes are shown in  
215Figures 5 and 6. Although three  $M 4+$  events are relatively small in magnitude, their slip patterns  
216are more complex than expected, with each event involving several slip patches. As mentioned  
217above, the  $M 5$  earthquake slipped on two relatively discrete areas, with the inverted maximum  
218slip around 15 cm and the final moment magnitude of  $M_w 4.9$  (Figure 5d). After it ruptured for  
219the first 0.5 -1 s, the rupture slowed down and paused for around 0.5 s before further propagation  
220along the NE side of the Cushing fault (Figure 5d and 6d). Comparing the slip contours of four  
221 $M 4+$  earthquakes (Figure 5e), their slip patches seem to partially complement with each other,  
222with minor overlap. The hypocenter of the  $M_w 4.9$  event is surrounded by the slip patches of  
223three former  $M 4+$  events.

224 With the inverted slip models, we computed Coulomb stress changes on the right-lateral  
225strike-slip fault for four earthquakes, using the Coulomb3 software (Toda et al., 2011). Similar  
226to previous studies (Stein et al., 1992; Toda et al., 2011), we used an effective coefficient of  
227friction of 0.4. We summed the Coulomb stress change for each main event, assuming that any  
228succeeding earthquake is affected by the cumulative stress changes caused by previous  
229earthquakes. For example, the 10/10/2015  $M_w 4.3$  event could be affected by the cumulative  
230Coulomb stress change from 09/28/2015  $M_w 4.1$  and 09/25/2015  $M_w 4.0$  event. As shown in  
231Figure 7, we found that most of aftershocks and subsequent  $M 4+$  earthquake occurred near the  
232boundary between the stress drop and stress increase areas. Although some uncertainties of  
233seismicity relocations and finite fault slip inversion may still remain, it suggests that Coulomb

234stress changes from previous earthquakes played an important role in triggering subsequent  
235earthquakes.

236 The obtained maximum stress drops for these four events are: 0.6, 1, 2 and 8 MPa,  
237respectively and the average stress drops are even lower. They are relatively low compared with  
238the average value of 14 MPa (Atkinson and Boore, 2006) or 18-25 MPa (Boore et al., 2010) for  
239central and eastern North American earthquakes. On the other hand, these stress drops are  
240comparable with the values from injection-induced earthquakes in other regions. For example,  
241Justinic et al. (2013) obtained an average stress drop of about 4.3 MPa for seven injection-  
242induced earthquakes in Cleburne, Texas. Wu et al. (2018) also found an average stress drop of  
2432.0 MPa for induced earthquakes in Oklahoma. However, with the same spectral ratio methods,  
244Huang et al. (2017) found that induced earthquakes have a comparable median stress drop to  
245shallow tectonic earthquakes in the central United States. Similarly, Daniels et al. (2020) used  
246the special ratio method and found that the 2014/02/15 M4.1 South Carolina earthquake and its  
247M3.0 aftershock (most likely natural events) had stress drop values of 3.75 and 4.44 MPa,  
248respectively. They argued that most injection-induced earthquakes (and the 2014 South Carolina  
249earthquake) were shallow (~3-5 km depth), and shallow earthquakes generally have lower stress  
250drops than earthquakes at larger depth (Shearer et al., 2006).

#### 2515. **Water Disposal and Stress Transfer**

252The Arbuckle group is the deepest sedimentary layer overlying the crystalline basement  
253throughout Oklahoma (Murray et al., 2014). Hence, it is a favorable formation for wastewater  
254disposal. Near Cushing, all disposal wells within 10 miles from hypocenters of four M4-5 events  
255inject wastewater into the Arbuckle group at ~1.2–2.0 km at depth. This is supported by

256checking the minimum and maximum depth of well completions (Figure 8b). The closest four  
257injection wells, within 3 miles, are all located to the north and west of four M4-5 epicenters  
258(Figure 1b). Analysis of OCC's monthly injection rate for the disposal wells within epicentral  
259distance of 3, 6 and 10 miles (Figure 1a), shows that injection rate increased gradually since  
2602011 and remained at a high level from January 2014 to September 2015 (Figure 8a). Most of the  
261injection data in 2013 is missing, due to the lost contact with an operation company that went  
262bankrupted in 2013 (private communication with OCC, 02/2019). The monthly injection into  
263Arbuckle group reduced twice, in 2015 after the three M4+ events and in 2016 after the M 5  
264event. The Arbuckle injection of four closest wells, within 3 miles, dropped to zero since October  
2652015. However, a large amount of water started to be injected into a shallower formation after  
266October 2015, for all injection wells within epicentral distance of 10 miles.

267       At present, without a good estimation of the permeability for the Arbuckle group, other  
268shallow formations, the basement and active fault zones, it is challenging to perform a realistic  
269simulation for water diffusion process or calculate the pore pressure and stress perturbation due  
270to fluid injection. Hence, it would be difficult to examine the causal relationship between the  
271seismic activity and water diffusion effect. Generally, water diffusion from nearby injection wells  
272since 2011 could gradually increase the pore pressure and reduce the fault strength on the  
273Cushing fault, leading to a critically stressed fault with increased seismic activity. We analyzed  
274the variance of seismicity rate from 2011 to 2020, within epicentral distance of 10 miles and the  
275magnitude completeness  $M_c$  is  $M 2.3$  (Figure S7). The seismicity rate surged since 2014,  
276consistent with the increased water injection rate after 2014 (Figure 8a). As mentioned before, an  
277injection reduction operation was imposed by OCC since October 2015, immediately after three  
278M 4+ events occurred. In addition, after the M 5 event in November 2016, the Arbuckle injection

279dropped to a very low level. The average seismic rate was lower since then, consistent with the  
280reduction of injection operation.

281       Foreshocks of the Cushing sequence started from 09/15/2015, three days before the  
28209/18/2015 M4.1 event, and in the following one month seismicity showed a bilateral migration  
283pattern along fault AA'(e.g., Figure 2h). We plotted the expected fluid diffusion curves with the  
284following equation:  $r = \sqrt{4\pi Dt}$ , where  $r$  is distance to the starting point of seismicity along  
285AA' and  $t$  is the time lapse. The seismicity in the foreshock sequence (i.e., from 09/15/2015 to  
286before the 09/18/2015 M4.1 event) expanded rapidly along the strike at the beginning, which  
287might be related with the Coulomb stress triggering to be discussed later. Hence, we set the  
288migration starting point of seismicity at point O and P along fault AA' on 09/15/2015 (Figure 2h).  
289The seismicity migrated from O towards A direction and migrated from P towards A' direction on  
290the other side. As shown in Figure 2h, the corresponding  $D$  values range from 0.05 to 0.1 m<sup>2</sup>/s  
291from the relocated catalog of Schoenball and Ellsworth (2017a). If we use the OGS (Walter et  
292al.,2019) and the template matching (Skoumal et al., 2019) catalogs, the corresponding  $D$  values  
293are in the range of 0.05–0.1 m<sup>2</sup>/s (Figure S1) and 0.12–0.22 m<sup>2</sup>/s (Figure S2), respectively. These  
294numbers are roughly within the range of estimations for the entire Oklahoma and Southern  
295Kansas (Schoenball and Ellsworth, 2017b), and smaller than those in volcanic regions (Shelly et  
296al., 2013a, 2013b). Such a rapid expansion of seismicity generally suggests a triggering by fluid  
297pressure diffusion (Shapiro et al., 1997; Hainzl, 2004). However, the seismic migration might be  
298related with bilateral aseismic slip after each M 4+ event, whose effect is difficult to be evaluated  
299without geodetic data.

300       After we analyzed the evolution of seismicity along fault CC', DD' and AA', we calculated  
301the Coulomb stress changes caused by several sequences (Figure 9), using an effective friction

302coefficient  $\mu' = 0.4$ . The Coulomb stress changes are resolved on the right-lateral fault striking  
30360 degrees at depth of 3 km, using the centroid location and mechanism information of the two  
304M4 earthquakes on fault CC' (2014) from McNamara et al. (2015). We found that the seismic  
305swarm during 2014 and 2015 (marked as DD' in Figure 2b) to the northwest of the two M4  
306events is located within the Coulomb stress increase area (Figure 9c), indicating that they were  
307likely triggered by static stress change after two M4 earthquakes. This inference is also  
308consistent with their right-lateral focal mechanisms (Figure S3). The western end of the Cushing  
309fault AA' is also within the Coulomb stress increase area. We also calculated the Coulomb stress  
310change caused by the seismic swarm (the largest event has a magnitude 3.4) and found that it  
311causes a subtle stress increase ( $\sim 2\text{-}5$  kPa) on the Cushing fault (Figure 9e-f), especially covered  
312the zone of four hypocenters of the Cushing earthquake sequence. The cumulative Coulomb  
313stress change on the Cushing fault, as shown by the map view and depth section in Figure 9d-e,  
314illustrates that the foreshocks of the 2015-2016 Cushing sequence (i.e., between 09/15/2015 and  
31509/18/2015) are located close to the boundary of stress increase and stress drop areas. If we used  
316smaller effective friction coefficient  $\mu'$ , for example 0.1 (Figure S8), all foreshocks and the  
317hypocenters of Cushing earthquake sequence fell within the Coulomb stress increase area. This is  
318because with a near zero  $\mu'$ , the Coulomb stress on fault AA' is less affected by the normal  
319stresses and mostly affected by the shear stress (Figure 9a-b). Hence, the resulting Coulomb  
320stress increase zone is shifted slightly towards the eastern side along fault AA'. On the other  
321hand, if a higher effective friction coefficient is used, for example 0.68 (Figure S9) as used in  
322Qin et al. (2018), the Coulomb stress increase area is shifted to the western side along fault AA'  
323and most of foreshocks and M4+ hypocenters are included in the Coulomb stress decrease area  
324(i.e., stress shadow). In fluid injection regions in Oklahoma, we expect presence of high fluid

325 pressures, which would result in low effective friction coefficient  $\mu'$ . Hence, we argue that a  
326 relatively small value  $\mu'$  should be used, which would also favor the interpretation that the 2015-  
327 2016 Cushing sequence was likely triggered by Coulomb stress changes from sequences a few  
328 kilometers in the south.

## 3296. Discussion

330 The evolution of seismicity is rather complicated, which migrated from an unmapped fault  
331 (CC') in the south to a nearby unmapped fault (DD'), and then to the AA' Cushing fault on the  
332 north. Such evolution can be qualitatively explained by the static Coulomb stress transfer.  
333 Because the Coulomb stress change is on the order of a few KPa, we argue that the areas around  
334 the hypocenters of the Cushing sequence are already critically stressed. In addition, the stress  
335 transfer originates from the fault further away from water injection wells towards the fault close  
336 to the injections well, instead of the opposite direction. When the foreshock sequence started 3  
337 days before the first M4.1 event, the seismicity front expands outward with time following  $\sqrt{t}$ ,  
338 consistent with being driven by fluid diffusion (Shapiro *et al.*, 1997; Hainzl, 2004). In addition,  
339 our finite-fault inversion results suggest that the slip regions of four M4+ events mostly  
340 complemented with each other, and the next event generally started at the edge of the previously  
341 ruptured region. Putting together, these results suggest a combined effects of Coulomb stress  
342 changes at different space-time scales, combined with fluid diffusions in driving the entire  
343 Cushing earthquake sequences.

344 McGarr *et al.* (2017) suggested the possibility of another M > 5 earthquakes to occur near  
345 Cushing city in the future, based on the large amount of total injection volume. By analyzing the  
346 seismicity pattern, we found that seismicity remains active along fault AA' after the M 5

347mainshock, as evidenced by several small earthquake swarms occurred in 2016, 2017 and 2019,  
348near the hypocenter of M 5 mainshock (Figure S1g). In addition, our Coulomb stress calculations  
349suggested that a region to the SW side and the central part (Figure 7d) of the Cushing fault are  
350positively stressed, and did not rupture during the recent sequence. So it is likely a possible  
351source region for future earthquakes. However, the overall injection volume and the seismicity  
352rate were steadily decreasing since 2016 (Figure 8). Hence, we argue that the seismic risk around  
353Cushing could be relatively reduced as compared with before, unless large stress is transferred  
354from the surrounding faults. Of course, our argument might be flawed since we did not consider  
355other unmapped faults (e.g., DD' in Figure 2) that are closer to the city.

356 In this study, the earthquake locations and finite fault inversion of  $M$  4+ events are possible  
357due to the availability of waveform data from a few seismometers very close the fault. In the near  
358future, dense seismic arrays near water disposal wells are essential for detecting weak seismic  
359events and studying rupture characteristics of induced earthquakes. In addition, water diffusion  
360and earthquake rupture simulation could be implemented with more realistic multiple fault  
361system and material properties, in order to better understand the relationship between fluid  
362injection and evolution of seismicity. These are beyond the scope of this study and will be  
363pursued in subsequent work.

364

## 3657. **Conclusion**

366 In this study, we analyzed the rupture process of four  $M$ 4-5 earthquakes, spatio-temporal  
367evolution of seismicity, water disposal history near Cushing city and stress transfer process  
368during the Cushing sequence. We found that the hypocenters of Cushing four earthquakes are

369very close and their inverted slip patches generally complement each other along fault AA'. Each  
370M 4+ earthquake in Cushing earthquake sequence was located on the boundary of Coulomb  
371stress change areas, implying a cascade Coulomb stress triggering effect. The 11/07/2016 *M*<sub>w</sub> 4.9  
372mainshock could be triggered by the cumulative Coulomb stress increase caused by three  
373previous M 4+ earthquakes from September and October 2015, though the mainshock occurred  
374one year later after the three M 4+ earthquakes. Before the Cushing earthquake sequence, the  
375seismicity migrated from unmapped faults CC' to DD' and then to the Cushing fault AA'. The  
376foreshock sequence of Cushing earthquake sequence starting three days before the first M4  
377earthquake, and occurred in the Coulomb stress increase region. The water injection activity on  
378northwest of Cushing increased the fluid pressure on the Cushing fault, making it a critically  
379stressed fault more susceptible for static stress triggering by seismic activities along the  
380upmapped faults CC' and DD'. The seismic bilateral expansions during the Cushing earthquake  
381sequence also suggest a role by fluid diffusion. While the southwestern and central part of the  
382Cushing fault are in the zones with positive Coulomb stress changes and remain un-ruptured, the  
383overall injection volume and background seismicity around Cushing have reduced since 2016.  
384Hence, the seismic risk around Cushing is further reduced as compared with before.

385

### 386**Acknowledgement and Data**

387The seismic waveform data are downloaded from IRIS Data Management Center  
388([http://ds.iris.edu/wilber3/find\\_event](http://ds.iris.edu/wilber3/find_event)). Earthquake catalog in this study is from National  
389Earthquake Information Center (<https://earthquake.usgs.gov/earthquakes/search/>) and Oklahoma  
390Geological Survey (OGS, [https://ogsweb.ou.edu/eq\\_catalog/](https://ogsweb.ou.edu/eq_catalog/)). Fault plane solutions are obtained  
391from OGS. Information on well completions and monthly injection data are downloaded from

392Oklahoma Corporation Commission (<http://www.occeweb.com/og/ogdatafiles2.htm>). Some figures  
393are made using Generic Mapping Tools ([www.soest.hawaii.edu/gmt](http://www.soest.hawaii.edu/gmt), last accessed January 2017;  
394Wessel and Smith 1998). This research is supported by National Natural Science Foundation of  
395China (Grant Number: 41304040) and US National Science Foundation (Grant Number:  
3961818611). Thanks for inspiring discussion with Dawid Szafranski and Benchun Duan, from  
397Texas A&M University, about water diffusion. This manuscript benefits from useful comments  
398by Xiaowei Chen from University of Oklahoma and Xiaofeng Meng from University of  
399Southern California.

400

#### 401**Reference:**

402Atkinson G. M., and Boore D. M., 2006. Earthquake ground-motion prediction equations for  
403 eastern North America, *Bull. Seismol. Soc. Am.*, 96, 2181–2205, doi:10.1785/0120050245.

404Bassin, C., G. Laske, and G. Masters, 2000. The current limits of resolution for surface wave  
405 tomography in North America, *Eos Trans. AGU*, **81**(48), Fall Meet. Suppl., Abstract S12A–  
406 03.

407Boore D. M., Campbell K. W., and Atkinson G. M., 2010. Determination of stress parameters for  
408 eight well-recorded earthquakes in eastern North America, *Bull. Seismol. Soc. Am.*, 100,  
409 1632–1645, doi:10.1785/0120090328.

410Brocher, T.A., 2005. Empirical relations between elastic wavespeeds and density in the Earth's  
411 crust. *Bull. Seismol. Soc. Am.*95, 2081–2092. <http://dx.doi.org/10.1785/0120050077>.

412Chen X. et al., 2017. The Pawnee earthquake as a result of the interplay among injection, faults  
413 and foreshocks, *Scientific Reports*, 7:4945, DOI:10.1038/s41598-017-04992-z.

414Chen, X., Haffener, J., Goebel, T. H. W., Meng, X., Peng, Z., and Chang, J.C., 2018. Temporal  
415 correlation between seismic moment and injection volume for an induced earthquake  
416 sequence in central Oklahoma. *Journal of Geophysical Research: Solid Earth*, 123, 3047–  
417 3064.<https://doi.org/10.1002/2017JB014694>.

418Daniels, C., Z. Peng, Q. Wu, S. Ni, X. Meng, D. Yao, L. S. Wagner, and K. M. Fischer, 2020. The  
419 15 February 2014 Mw 4.1 South Carolina Earthquake Sequence: Aftershock Productivity,  
420 Hypocentral Depths, and Stress Drops, *Seismol. Res. Lett.* 91, 452–464, doi:  
421 10.1785/0220190034.

422Ellsworth W. L., 2013. Injection Induced earthquakes, *Science* 341, 1225942. DOI:  
423 10.1126/science.1225942

424Goebel, T. H. W., Weingarten, M., Chen, X., Haffener, J., and Brodsky, E. E., 2017. The 2016  
425 Mw5.1 Fairview, Oklahoma earthquakes: Evidence for long-range poroelastic triggering at  
426 >40 km from fluid disposal wells. *Earth and Planetary Science Letters*, 472, 50–61.  
427 <https://doi.org/10.1016/j.epsl.2017.05.011>.

428Grandin R, Vallée M, Lacassin R., 2017. Rupture Process of the Mw 5.7 Pawnee, Oklahoma,  
429 Earthquake from Sentinel-1 InSAR and Seismological Data[J]. *Seismol. Res. Lett.*,88

430Hartzell, S. H., and T. H. Heaton, 1983. Inversion of strong ground motion and teleseismic  
431 waveform data for the fault rupture history of the 1979 Imperial Valley, California,  
432 earthquake, *Bull. Seismol. Soc. Am.*, 73(6A), 1553–1583.

433Hainzl, S., 2004. Seismicity patterns of earthquake swarms due to fluid intrusion and stress  
434 triggering, *Geophys. J. Int.*, 159, 1090–1096.

435Hincks T. , Aspinall W. , Cooke R. , Gernon T., 2018. Oklahoma's induced seismicity strongly  
436 linked to wastewater injection depth, *Science*, 359(6381), 1251–1255,  
437 doi.org/10.1126/science.aap7911.

438Huang, Y., Ellsworth, W. L., & Beroza, G. C., 2017. Stress drops of induced and tectonic  
439 earthquakes in the Central United States are indistinguishable. *Science Advances*, 3(8),  
440 e1700772. <https://doi.org/10.1126/sciadv.1700772>.

441Justinic A. H., Stump B., Hayward C., and Frohlich C., 2013. Analysis of the Cleburne, Texas,  
442 earthquake sequence from June 2009 to June 2010, *Bull. Seismol. Soc. Am.*, 103(6), 3083–  
443 3093, doi:10.1785/0120120336.

444Keranen, K., H. M. Savage, G. Abers, and E. S. Cochran, 2013. Potentially induced earthquakes  
445 in Oklahoma, USA: Links between wastewater injection and the 2011  $M_w$  5.7 earthquake  
446 sequence, *Geology*, 41, 699–702, doi:10.1130/G34045.1.

447Keranen, K. M., M. Weingarten, G. A. Abers, B. A. Bekins, and S. Ge, 2014. Induced  
448 earthquakes. Sharp increase in central Oklahoma seismicity since 2008 induced by massive  
449 wastewater injection, *Science*, 345(6195), 448–51.

450Klein, F. W., 2014. User's guide to HYPOINVERSE-2000, a Fortran program to solve for  
451 earthquake locations and magnitude, U.S. Geol. Surv. Open-File Rept. 02-171, revised June  
452 2014.

453 Marsh, S., Holland A., 2016. Comprehensive Fault Database and Interpretive Fault Map of  
454 Oklahoma, OF2-2016.

455 McGarr, A., & Barbour, A. J., 2017. Wastewater disposal and the earthquake sequences during  
456 2016 near Fairview, Pawnee, and Cushing, Oklahoma. *Geophysical Research Letters*, 44,  
457 9330–9336. <https://doi.org/10.1002/2017GL075258>.

458 McNamara, D. E., et al., 2015. Reactivated faulting near Cushing, Oklahoma: Increased potential  
459 for a triggered earthquake in an area of United States strategic infrastructure, *Geophys. Res.*  
460 *Lett.*, 42, 8328–8332, doi:[10.1002/2015GL064669](https://doi.org/10.1002/2015GL064669).

461 Murray, K. E., 2014. Class II Underground Injection Control Well Data for 2010–2013 by  
462 Geologic Zones of Completion. Oklahoma Geological Survey Open File Report OF1-2014,  
463 32.

464 Mogi, K., H. Mochizuki, and Y. Kurokawa, 1990. Changes in hot springs in the Usami-Ito area  
465 related to the 1989 Ito-oki earthquake swarm and submarine eruption, Rep. Coord. Comm.  
466 Earthq. Predict., 43, 290-299.

467 Oklahoma Corporation Commission, 2015. Media advisory—Cushing earthquakes. [Available at  
468 [http://www.occeweb.com/News/10-19-15CUSHING\\_2.pdf](http://www.occeweb.com/News/10-19-15CUSHING_2.pdf).]

469 Pei, S., Peng, Z., and Chen, X., 2018. Locations of injection-induced earthquakes in Oklahoma  
470 controlled by crustal structures. *J. Geophys. Res. Solid Earth*, 123, 2332–2344,  
471 doi.org/10.1002/2017JB014983.

472Qin, Y., Chen, X., Carpenter, B. M., & Kolawole, F., 2018. Coulomb stress transfer influences  
473 fault reactivation in areas of wastewater injection. *Geophysical Research Letters*, 45,  
474 11,059–11,067.

475Schoenball, M., & Ellsworth, W., 2017a. Waveform relocated earthquake catalog for Oklahoma  
476 and Southern Kansas illuminates the regional fault network. *Seismological Research  
477 Letters*, 88(5), 1252–1258. <https://doi.org/10.1785/0220170083>.

478Schoenball, M., & Ellsworth, 2017b. W., A systematic assessment of the spatiotemporal  
479 evolution of fault activation through induced seismicity in Oklahoma and southern Kansas.  
480 *Journal of Geophysical Research: Solid Earth*, 122, 10,189–10,206.  
481 <https://doi.org/10.1002/2017JB014850>.

482Segall P., and Lu S., 2015. Injection-induced seismicity: Poroelastic and earthquake nucleation  
483 effects, *J. Geophys. Res. Solid Earth*, 120, 5082–5103, doi:10.1002/2015JB012060.

484Shapiro, S. A., E. Huenges, and G. Borm, 1997. Estimating the crust permeability from fluid-  
485 injection-induced seismic emission at the KTB site, *Geophys. J. Int.*, 131, F15–F18.

486Shearer, P. M., G. A. Prieto, and E. Hauksson, 2006. Comprehensive analysis of earthquake  
487 source spectra in southern California, *J. Geophys. Res.*, 111, B06303,  
488 doi:10.1029/2005JB003979.

489Shelly, D. R., S. C. Moran, and W. A. Thelen, 2013a. Evidence for fluid-triggered slip in the  
490 2009 Mount Rainier, Washington earthquake swarm, *Geophys. Res. Lett.*, 40, 1506–1512,  
491 doi:10.1002/grl50354.

492 Shelly, D. R., D. P. Hill, F. Massin, J. Farrell, R. B. Smith, and T. Taira, 2013b. A fluid-driven  
493 earthquake swarm on the margin of the Yellowstone caldera, *J. Geophys. Res. Solid Earth*,  
494 118, 4872–4886, doi:10.1002/jgrb.50362.

495 Skoumal, R. J., Kaven, J. O., & Walter, J. I., 2019. Characterizing seismogenic fault structures in  
496 Oklahoma using a relocated template-matched catalog. *Seismological Research Letters*,  
497 90(4), 1535–1543. <https://doi.org/10.1785/0220190045>.

498 Stein, R. S., G. C. P. King, and J. Lin, 1992. Change in failure stress on the southern San Andreas  
499 fault system caused by the 1992 magnitude = 7.4 Landers earthquake, *Science*, 258, 1328–  
500 1332.

501 Sumy, D. F., Cochran E. S., Keranen K. M., Wei M., and Abers G., 2014. Observations of static  
502 Coulomb stress triggering of the November 2011 M 5.7 Oklahoma earthquake sequence, *J.*  
503 *Geophys. Res. Solid Earth*, 119, 1904–1923, doi:10.1002/2013JB010612.

504 Sun X., and Hartzell S., 2014. Finite- fault slip model of the 2011 Mw 5.6 Prague, Oklahoma  
505 earthquake from regional waveforms, *Geophys. Res. Lett.*, 40, 4207–4213,  
506 doi:10.1002/2014GL060410.

507 Talwani, P., Chen, L. & Gahalaut, K, 2007. Seismogenic permeability, ks. *Journal of Geophysical*  
508 *Research: Solid Earth* 112, 1–18.

509 Taylor J. et al., 2017. M5.0 Cushing, Oklahoma, USA Earthquake on November 7, 2016, EERI  
510 Earthquake Reconnaissance Team Report.

511 Toda, S., R. S. Stein, V. Sevilgen, and J. Lin, 2011. Coulomb 3.3 Graphic-Rich Deformation and  
512 Stress-Change Software for Earthquake, Tectonic, and Volcano Research and Teaching –  
513 User Guide, *U. S. Geol. Surv. Open-File Rep. 2011-1060*.

514 Waldhauser, F., and W. L. Ellsworth, 2000. A double-difference earthquake location algorithm:  
515 Method and application to the northern Hayward fault, California, *Bull. Seismol. Soc. Am.*  
516 90, no. 6, 1353–1368, doi: 10.1785/0120000006.

517 Walter, J. I., P. Ogwari, A. Thiel, F. Ferrer, I. Woelfel, J. C. Chang, A. P. Darold, and A. A.  
518 Holland, 2019. The Oklahoma Geological Survey Statewide Seismic Network, *Seismol.*  
519 *Res. Lett.* 91, 611–621, doi: 10.1785/0220190211.

520 Wei, S. *et al.*, 2015. The 2012 Brawley swarm triggered by injection-induced aseismic slip,  
521 *Earth and Planetary Science Letters* 422, 115-125.

522 Weingarten, M., S. Ge, J. W. Godt, B. A. Bekins, and J. L. Rubinstein, 2015. High-rate injection  
523 is associated with the increase in U.S. mid-continent seismicity, *Science*, 348(6241), 1336–  
524 1340, doi:[10.1126/science.aab1345](https://doi.org/10.1126/science.aab1345).

525 Wu, Q., Chapman, M. C., & Chen, X., 2018. Stress-drop variations of induced earthquakes in  
526 Oklahoma. *Bulletin of the Seismological Society of America*, **108**(3A), 1107–  
527 1123. <https://doi.org/10.1785/0120170335>.

528 Wu, Q., Chen, X., & Abercrombie, R. E., 2019. Source complexity of the 2015Mw 4.0 Guthrie,  
529 Oklahoma earthquake. *Geophysical Research Letters*, 46, 4674–4684.  
530 <https://doi.org/10.1029/2019GL082690>.

531 Yeck, W. L., G. P. Hayes, D. E. McNamara, J. L. Rubinstein, W. D. Barnhart, P. S. Earle, and H.

532 M. Benz, 2017. Oklahoma experiences largest earthquake during ongoing regional

533 wastewater injection hazard mitigation efforts, *Geophys. Res. Lett.*, **44**, 711–717.

534 Yue, H., and T. Lay, 2013. Source rupture models for the Mw 9.0 2011 Tohoku earthquake from

535 joint inversions of high-rate geodetic and seismic data, *Bull. Seismol. Soc. Am.*, **103**, 1242–

536 1255, doi:10.1785/0120120119.

537 Zhu L. and Ben-Zion Y., 2013. Parameterization of general seismic potency and moment tensors

538 for source inversion of seismic waveform data, *Geophys. J. Int.*, **194**, 839-843

539 Zhu, L., and L. Rivera, 2002. A note on the dynamic and static displacements from a point

540 source in multilayered media, *Geophys. J. Int.*, **148(3)**, 619– 627.

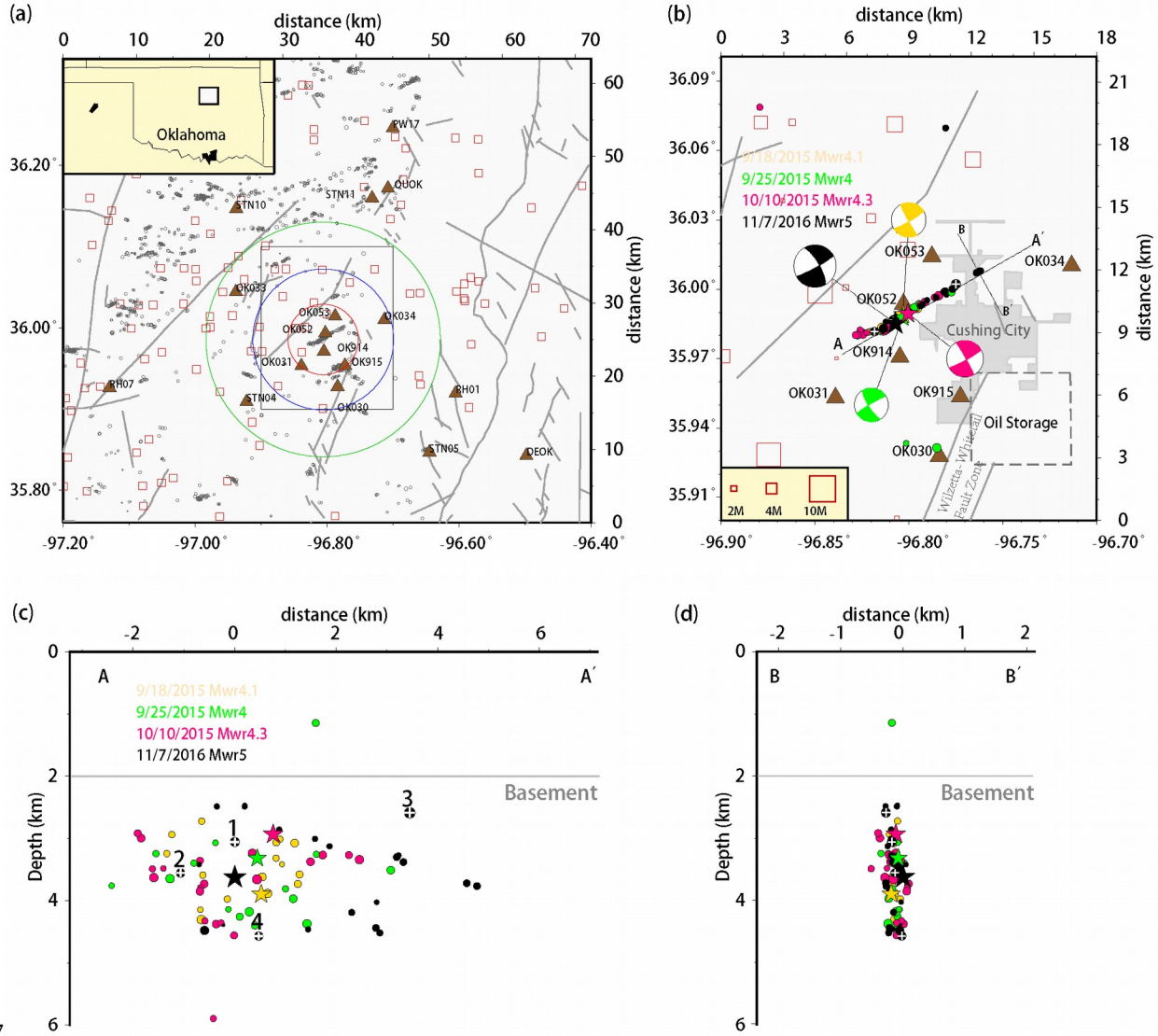
541

542

543

544

546 **Figures and Tables:**

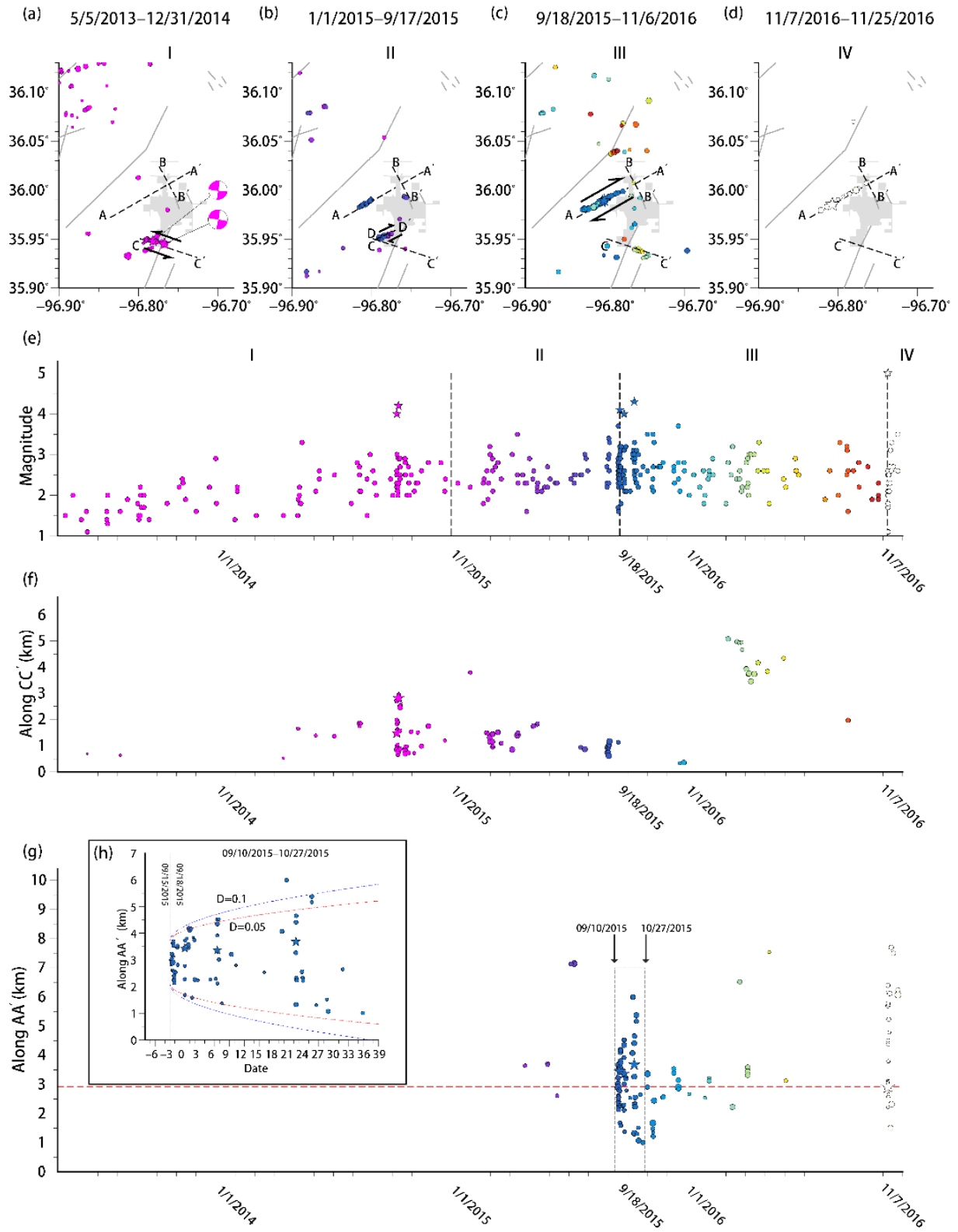


548 Figure 1. Seismicity near Cushing city, and seismic stations and disposal wells. (a) Seismicity  
 549 (grey circles) from May 2013 to November 2016 using the catalog from Schoenball and  
 550 Ellsworth (2017a). Disposal wells are indicated with red squares. Browns triangles show seismic  
 551 stations within 35km epicentral distance from hypocenters of Cushing earthquake sequence. Two  
 552 close stations OK052 and OK053 were available several days after the mainshock. Grey lines

553 show mapped faults from OGS database (Marsh and Holland, 2016). Red, blue and green circles  
554 denote 3, 6, and 10 miles radius, respectively. (b) A zoomed-in plot of the study region. Size of  
555 red squares (wells) is scaled with the total water injection volume from 2014 to 2018, in million  
556 barrels. Colored stars and circles show relocated  $M > 4$  earthquakes and their aftershocks (within  
557 20 days). Focal mechanisms are displayed as colored beach balls (parameters in Table 1). (c) A  
558 depth section of events along the AA' profile in (b). Four aftershocks denoted with white pluses  
559 are used as reference events for velocity structure calibration. (d) A depth section of events along  
560 the BB' profile in (b).

561

562



563

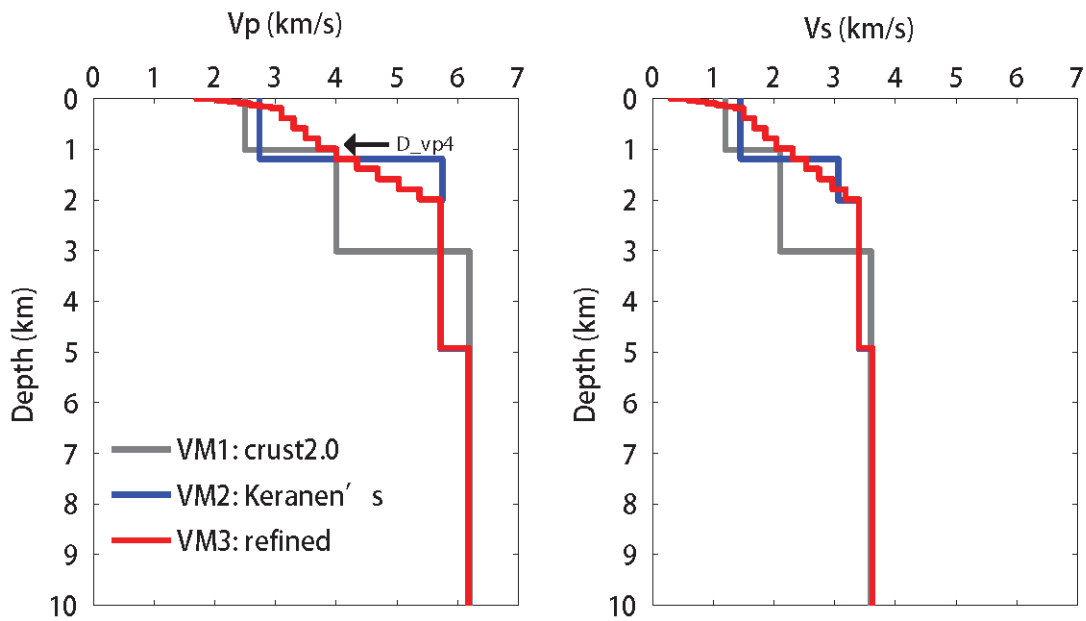
57

29

58

564Figure 2. Geographic distribution of seismicity (Schoenball and Ellsworth 2017a) for different  
565time stages (a) I: May 2013 to Dec. 31, 2014. The beachballs represent the focal mechanisms of  
566two M4 earthquakes happened in 2014 on south of Cushing fault AA'. (b) II: Jan.1, 2015 to  
567Sep.17, 2015 (c) III: Sep.18, 2015 to Nov. 6, 2016 (d) IV: Nov.7, 2016 to Dec.25, 2016. Faults  
568AA' and DD' are in right-lateral motions and fault CC' is in left-lateral motion. (e) Magnitude-  
569Time plot of seismicity during different time stages. (f) Evolution of the earthquake locations  
570along fault CC' vs time. (g) Evolution of earthquake locations along fault AA' vs time. The  
571horizontal red dashed line denotes the location of the M 5 mainshock hypocenter. (h) A zoomed-  
572in plot showing earthquake evolution within the dashed box in (g). Two colored dashed lines  
573show the fluid diffusion curves with diffusivity  $D=0.05$  (red) and  $D=0.1$  (blue).

574



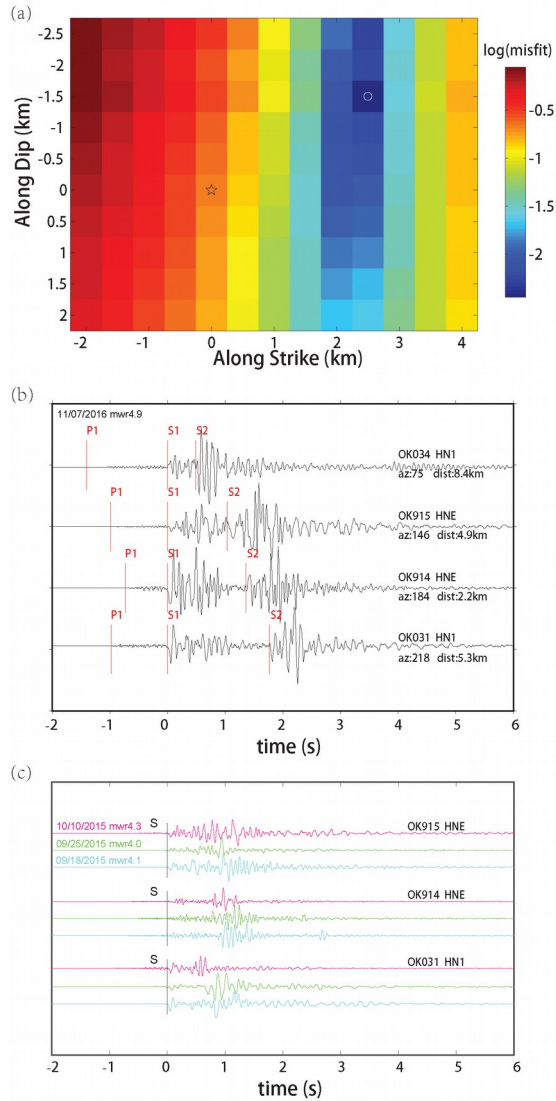
575

576 Figure 3. Vp and Vs velocity models used in this study (Gray, VM1: Crust2.0 models; Blue, VM2: Keranen

577 et al. (2013); Red, VM3: a refined version of Keranen's model). D\_vp4 is the grid searched depth of

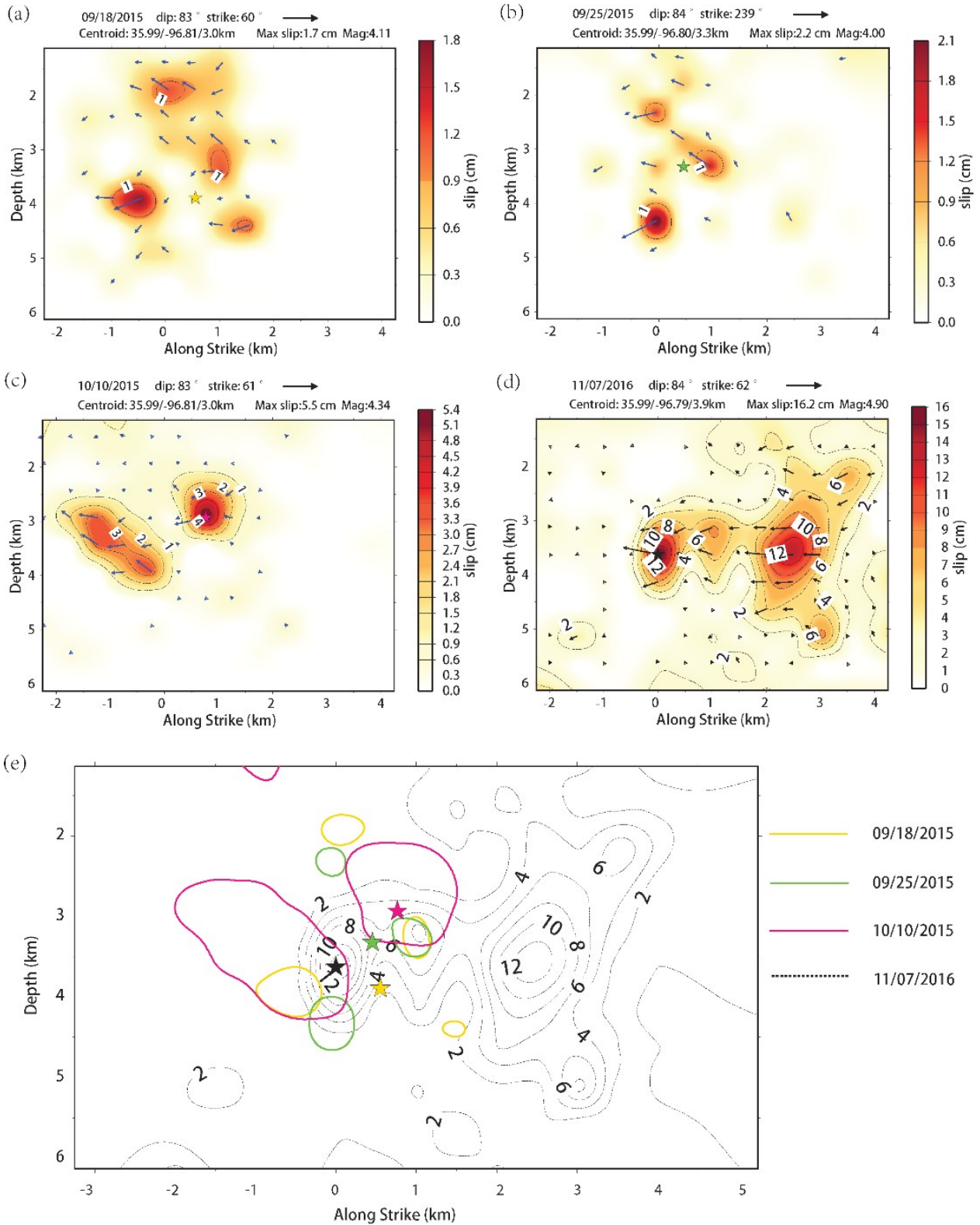
578  $V_p=4\text{km/s}$ .

579



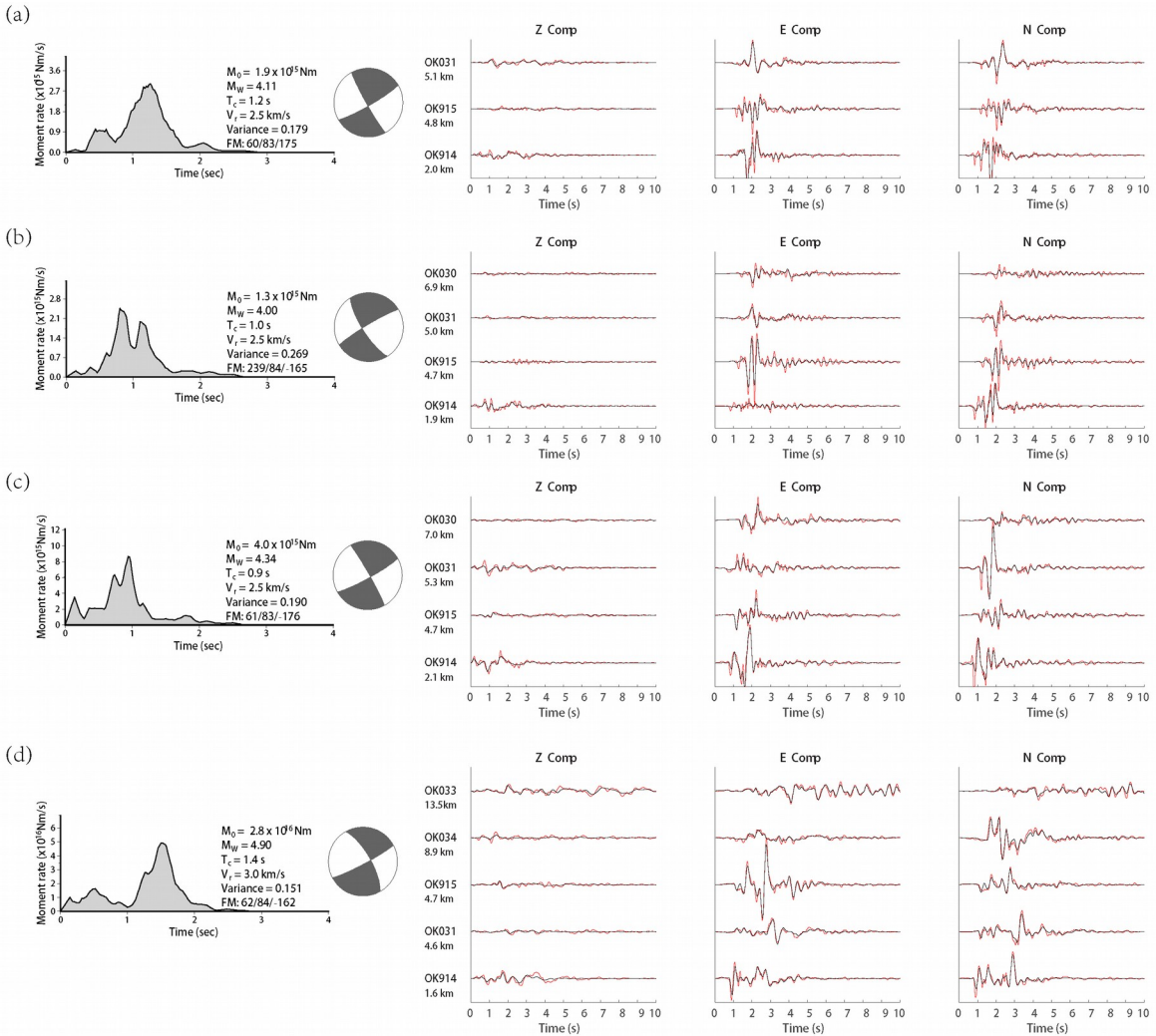
580

581 Figure 4. Modeling of the two sub-events of the M5 earthquake. (a) Location of the second sub-event  
 582 from fitting the differential S-wave arrival time of two sub-events. The black star is the hypocenter the  
 583 first sub-event and the white circle is the preferred location of the second sub-event. (b) Raw seismic  
 584 waveforms for the M5 mainshock on four stations. The P wave and S wave arrivals for the first sub-event  
 585 are labeled as P1 and S1. And S arrival for the second sub-event is labeled as S2, with S1 aligned at 0 s.  
 586 (c) Raw seismic waveforms for three M4+ earthquakes on three stations, with S arrival time aligned at 0  
 587 s.



590Figure 5. Rupture models from finite fault inversion of (a) the 09/18/2015  $M_w$  4.1, (b) the  
59109/25/2015  $M_w$  4.0, (c) the 10/10/2015  $M_w$  4.3, and (d) the 11/07/2016  $M_w$  4.9 earthquake. The  
592colored stars denote the hypocenters of four target earthquakes. The blue arrows in each panel  
593represents the inverted slip direction and magnitude at each cell. The centroid location, the  
594maximum slip and magnitude, and fault geometry information (dip and strike angles) are shown  
595on the top of each panel. (e) The 1 cm slip contours for three 2015  $M$  4+ events, and the full slip  
596contour for the 2016 mainshock.

597



598

599Figure 6. Source time function and seismic waveform fitting on nearby stations for (a) the 09/18/2015  
600event (b) the 09/25/2015 event (c) the 10/10/2015 event (d) the 11/07/2016 mainshock. The vertical (Z),  
601east (E) and north(N) components are displayed from left to right. Station code and epicentral distance  
602are also labeled.

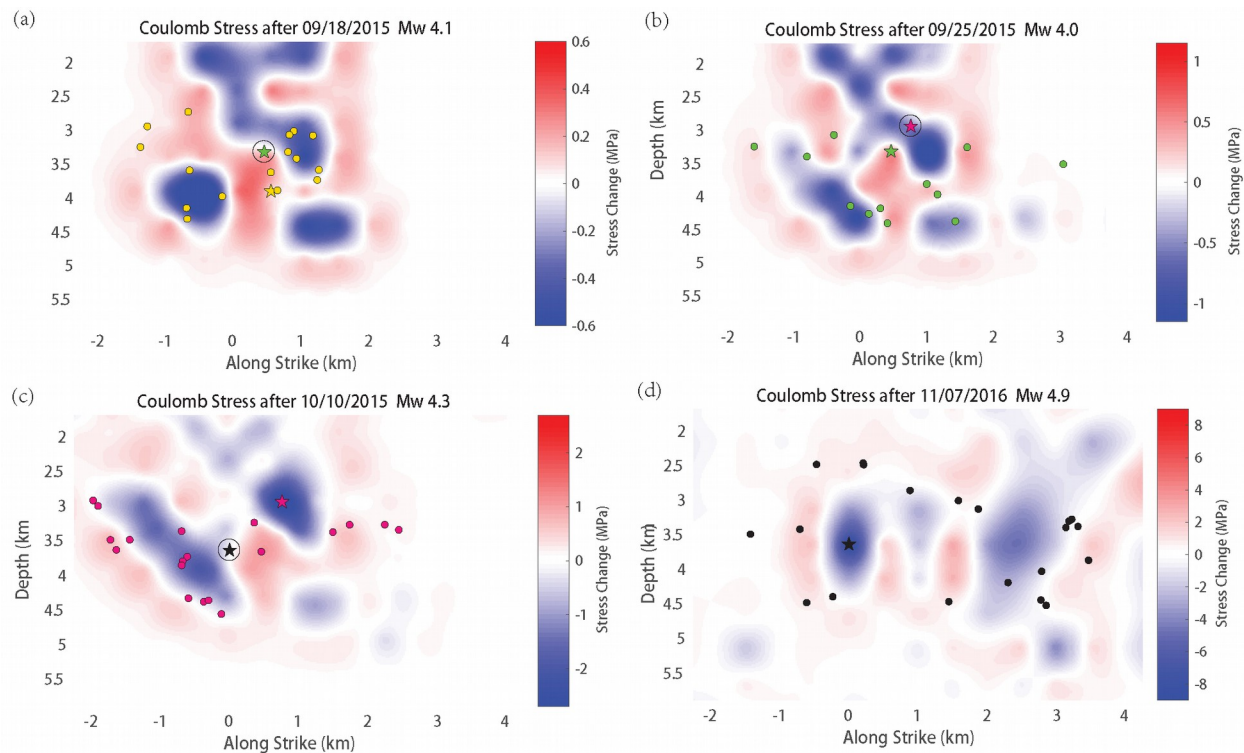
603

604

605

69

70

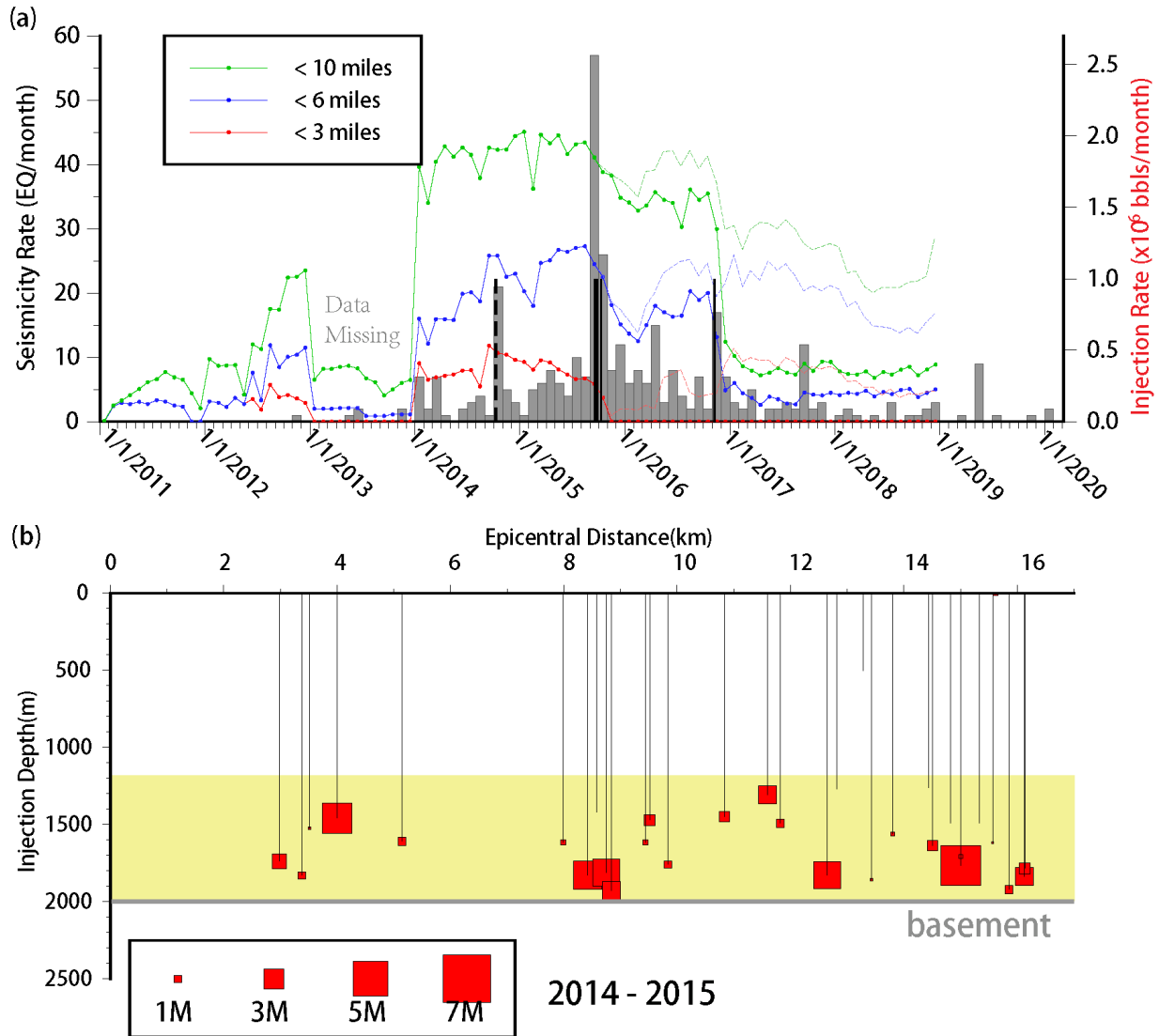


606

607Figure 7. (a) Cumulative Coulomb stress change on the causative fault, immediately after the  
 60809/18/2015 Mw 4.1 event, based on the finite fault model in Figure 3. The yellow star and dots  
 609are locations of the hypocenter and aftershocks of the 09/18/2015 event, while the circled green  
 610star represents hypocenter of the 09/25/2015 Mw 4.0 event. (b) Cumulative Coulomb stress  
 611change after adding the Coulomb stress change from the 09/18/2015 and 09/25/2015 events. The  
 612green star and dots are locations of hypocenter and aftershocks of the 09/25/2015 event, while  
 613the circled magenta star represents hypocenter of the 10/10/2015 Mw 4.3 event. (c) Cumulative  
 614Coulomb stress change after adding the Coulomb stress change from the 09/18/2015, 09/25/2015  
 615and 10/10/2015 events. The magenta star and dots are locations of hypocenter and aftershocks of  
 616the 10/10/2015 event, while the circled black star represents hypocenter location of the  
 61711/07/2016 M 5 event. (d) Cumulative Coulomb stress change after summing from the four M4+

618earthquakes in the Cushing sequence. The black star and dots are locations of hypocenter and  
619aftershocks of the 11/07/2016 event.

620



621

622 Figure 8. Water injection history in disposal wells near Cushing city and evolution of seismicity.

623 (a) Monthly water injection volume, from Jan. 2011 to Dec. 2018, of disposal wells within 3

624 miles (red line), 6 miles (blue line) and 10 miles (green line) from the 11/07/2016 mainshock

625 epicenter. The dashed lines represent the total monthly injection volume into the crust after

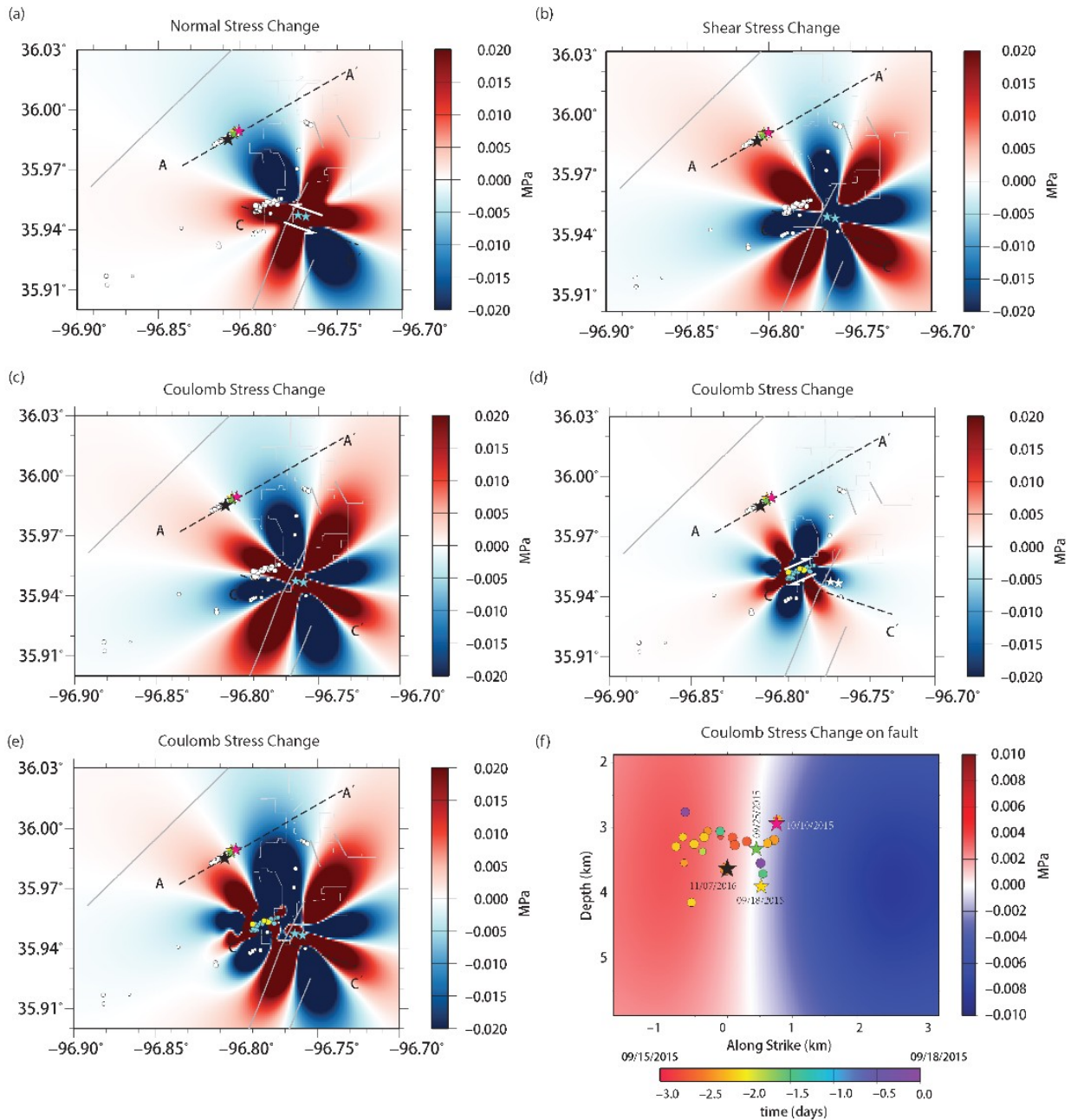
626 September 2015 and the solid lines represent volume injected into the Arbuckle group. Grey

627 bars are numbers of earthquakes in each month which occurred within 10 miles from the

628 mainshock epicenter, shown in Fig. 1a. Black vertical lines denote the four M > 4 earthquakes in

6292015-2016 and the dashed vertical line denote two  $M > 4$  earthquakes happened in Oct. 2014 to  
630the south of the Cushing fault. The water injection data were not available from 2013 to 2014  
631near Cushing area. (b) Well completion depths and injection volume in 2014 and 2015, of each  
632disposal wells within 10 miles from the M5 mainshock hypocenter. The red squares show depth  
633of the wells with size of the squares denoting total water injection volume at each well.

634



637Figure 9. Coulomb stress changes resolved on right-lateral fault, striking 60 degrees with  
 638effective friction coefficient on fault set as 0.4. (a) Normal stress change at depth of 3km, caused  
 639by two M4 left-lateral earthquakes (cyan stars) occurred in October 2014 south of Cushing city.  
 640The focal mechanisms and centroid locations of these two M4 earthquakes are from McNamara

641et al. (2015). The color saturation is set at a small value of 0.2 MPa, to better show small  
642Coulomb stress change for a larger area. Negative values mean clamping on the fault. (b) Shear  
643stress change at depth of 3 km, caused by two M4 left-lateral earthquakes occurred in October  
6442014 on the south of Cushing city. (c) Coulomb stress change at depth of 3 km, caused by two  
645M4 left-lateral earthquakes occurred in October 2014 south of Cushing city. (d) Coulomb stress  
646change at depth of 3 km, caused by many right-lateral strike-slip earthquakes (cyan circles)  
647occurred after two left-lateral M4 earthquakes in 2014 and before the Mw 4.1 09/18/2015  
648earthquake. The yellow circles are  $M > 3$  earthquakes shown in Figure S3. (e) Coulomb stress  
649change at depth of 3 km, contributed from the left-lateral and right-lateral earthquakes shown in  
650(c) and (d). (f) Coulomb stress change on the cross section along the AA' Cushing fault, caused  
651by summing contributions from both left-lateral and right-lateral earthquakes. The colored circles  
652are foreshocks occurred within three days before the 09/18/2015 Mw 4.1 event, with color of  
653circles representing their relative occurrence times. The locations of Cushing earthquake  
654sequence in this study are marked by colored stars and labelled by time.

655

656Table 1. Fault plane solutions of the four earthquakes from waveform inversion with the Cut and  
657Paste (CAP) method

Date (mm/dd/yyyy)	Magnitude ( $M_w$ )	Centroid Depth (km)	Nodal Plane 1 Strike(°)/Dip(°)/Rake(°)	Nodal Plane 2 Strike(°)/Dip(°)/Rake(°)
09/18/2015	4.08	4.0	60/83/175	151/86/7
09/25/2015	3.95	3.3	249/84/-165	148/76/-6
10/10/2015	4.32	3.6	61/83/-176	331/87/-7
11/07/2016	4.89	4.7	61/84/-162	330/73/-6

658

659

# **The 2015-2016 Earthquake Sequence in Cushing, Oklahoma driven by Coulomb Stress Changes and Fluid Diffusions**

Qingjun Meng <sup>1</sup>, Sidao Ni <sup>2</sup>, Zhigang Peng <sup>3,\*</sup>

<sup>1</sup> Department of Geology and Geophysics, Texas A&M University, College Station, TX, USA

([qimeng@tamu.edu](mailto:qimeng@tamu.edu))

<sup>2</sup> State Key Laboratory of Geodesy and Earth's Dynamics, Institute of Geodesy and Geophysics,

Chinese Academy of Sciences, Wuhan, China ([sdni@apm.ac.cn](mailto:sdni@apm.ac.cn))

<sup>3</sup> School of Earth and Atmospheric Sciences, Georgia Institute of Technology, Atlanta, GA, USA

([zpeng@gatech.edu](mailto:zpeng@gatech.edu))

Corresponding author: Zhigang Peng ([zpeng@gatech.edu](mailto:zpeng@gatech.edu))

## **Contents of this file**

Table S1-S2

Table S1. Information for four reference events

Event Number	Date (mm/dd/yyyy)	Time (hh:mm:ss.ss)	Magnitude (ML)	Latitude (°) (hypo2000)	Longitude (°) (hypo2000)	Depth (km) (hypo2000)	Depth (km) (Adjusted for Path Calibration)
1	11/10/2015	13:36:45.76	3.3	35.9867	-96.8082	3.06	2.4
2	11/11/2016	00:08:05.46	3.1	35.9817	-96.8183	3.56	3.0
3	11/22/2016	09:55:33.51	3.5	36.0023	-96.7750	2.59	2.6
4	11/24/2016	16:34:06.91	3.3	35.9875	-96.8027	4.57	5.1

Table S2. Velocity structure of the VM3 model, shown in Figure 3.

Thickness (km)	Vp (km/s)	Vs (km/s)
0.008	1.70	0.30
0.03	2.06	0.60
0.03	2.23	0.75
0.03	2.41	0.9
0.03	2.58	1.05
0.03	2.75	1.20
0.03	2.93	1.35
0.20	3.10	1.50
0.20	3.30	1.68
0.20	3.50	1.86
0.20	3.70	2.04
0.20	4.00	2.31
0.20	4.34	2.53
0.20	4.69	2.75
0.20	5.03	2.96
0.20	5.38	3.18
2.93	5.72	3.40
6.00	6.18	3.62
4.00	6.32	3.67
20.00	6.60	3.70
11.00	7.30	4.00
99.00	8.20	4.70



# **The 2015-2016 Earthquake Sequence in Cushing, Oklahoma driven by Coulomb Stress Changes and Fluid Diffusions**

Qingjun Meng <sup>1</sup>, Sidao Ni <sup>2</sup>, Zhigang Peng <sup>3,\*</sup>

<sup>1</sup> Department of Geology and Geophysics, Texas A&M University, College Station, TX, USA

([qimeng@tamu.edu](mailto:qimeng@tamu.edu))

<sup>2</sup> State Key Laboratory of Geodesy and Earth's Dynamics, Institute of Geodesy and Geophysics,

Chinese Academy of Sciences, Wuhan, China ([sdni@apm.ac.cn](mailto:sdni@apm.ac.cn))

<sup>3</sup> School of Earth and Atmospheric Sciences, Georgia Institute of Technology, Atlanta, GA, USA

([zpeng@gatech.edu](mailto:zpeng@gatech.edu))

Corresponding author: Zhigang Peng ([zpeng@gatech.edu](mailto:zpeng@gatech.edu))

## **Contents of this file**

Figure S1-S9

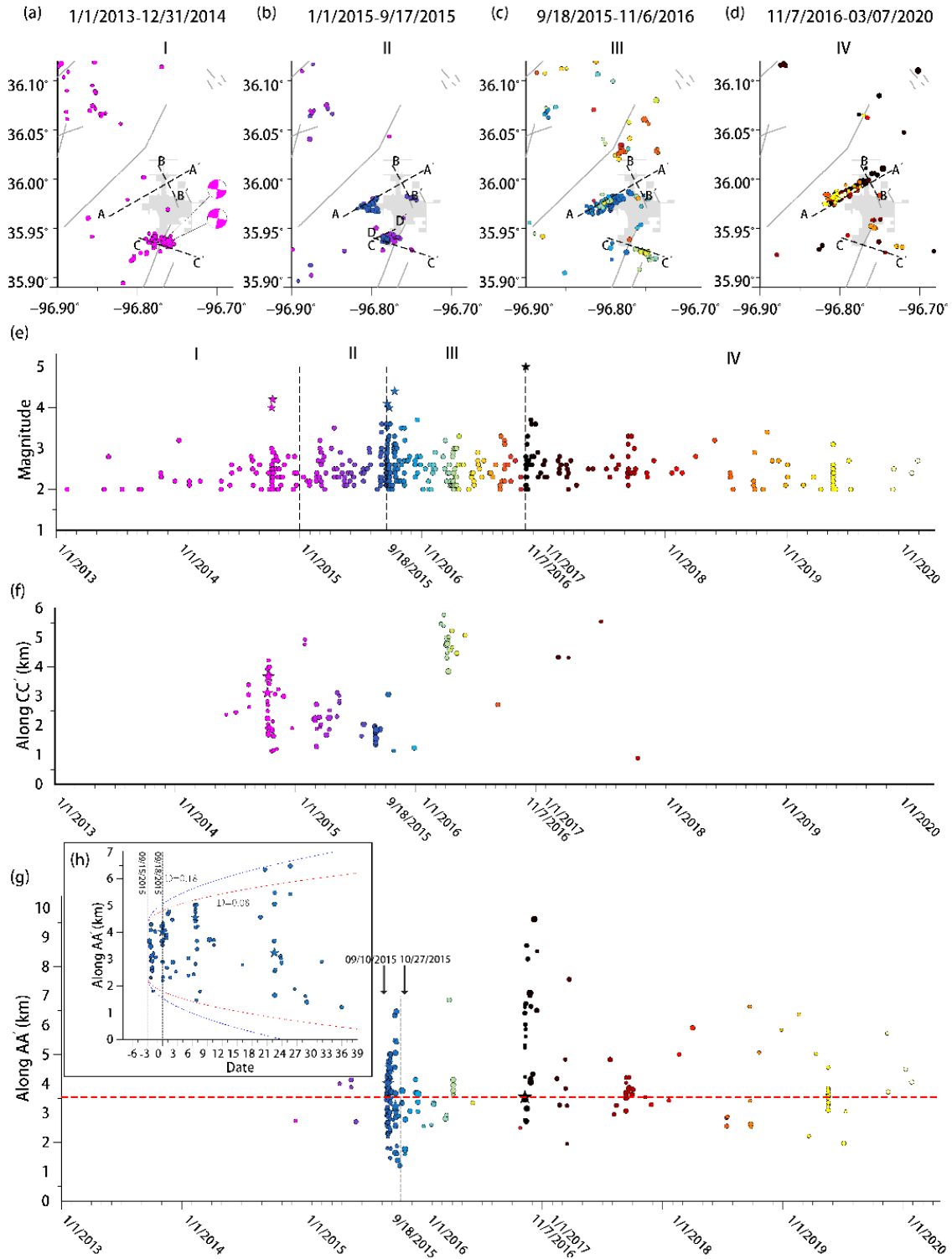


Figure S1. Geographic distribution of seismicity (OGS catalog) for different time stages (a) I: Jan. 1, 2013 to Dec. 31, 2014. The beachballs represent the focal mechanisms of two M4 earthquakes happened in

2014 on south of Cushing fault. (b) II: Jan.1, 2015 to Sep.17, 2015 (c) III: Sep.18, 2015 to Nov. 6, 2016 (d) IV: Nov.7, 2016 to Dec.25, 2016. Fault AA' and DD' are right lateral and fault CC' is left lateral. (e) Magnitude-Time plot of seismicity during each time stage I, II, III and IV. (f) Evolution of the earthquake locations along fault CC' vs time. (g) Evolution of the earthquake locations along fault AA' vs time. The horizontal red dashed line denotes the location of the M 5 mainshock hypocenter. (h) A zoomed-in plot showing earthquake evolution within the dashed box in (g). Two colored dashed lines show the fluid diffusion curves with diffusivity  $D=0.08$  (red) and  $D=0.18$  (blue).

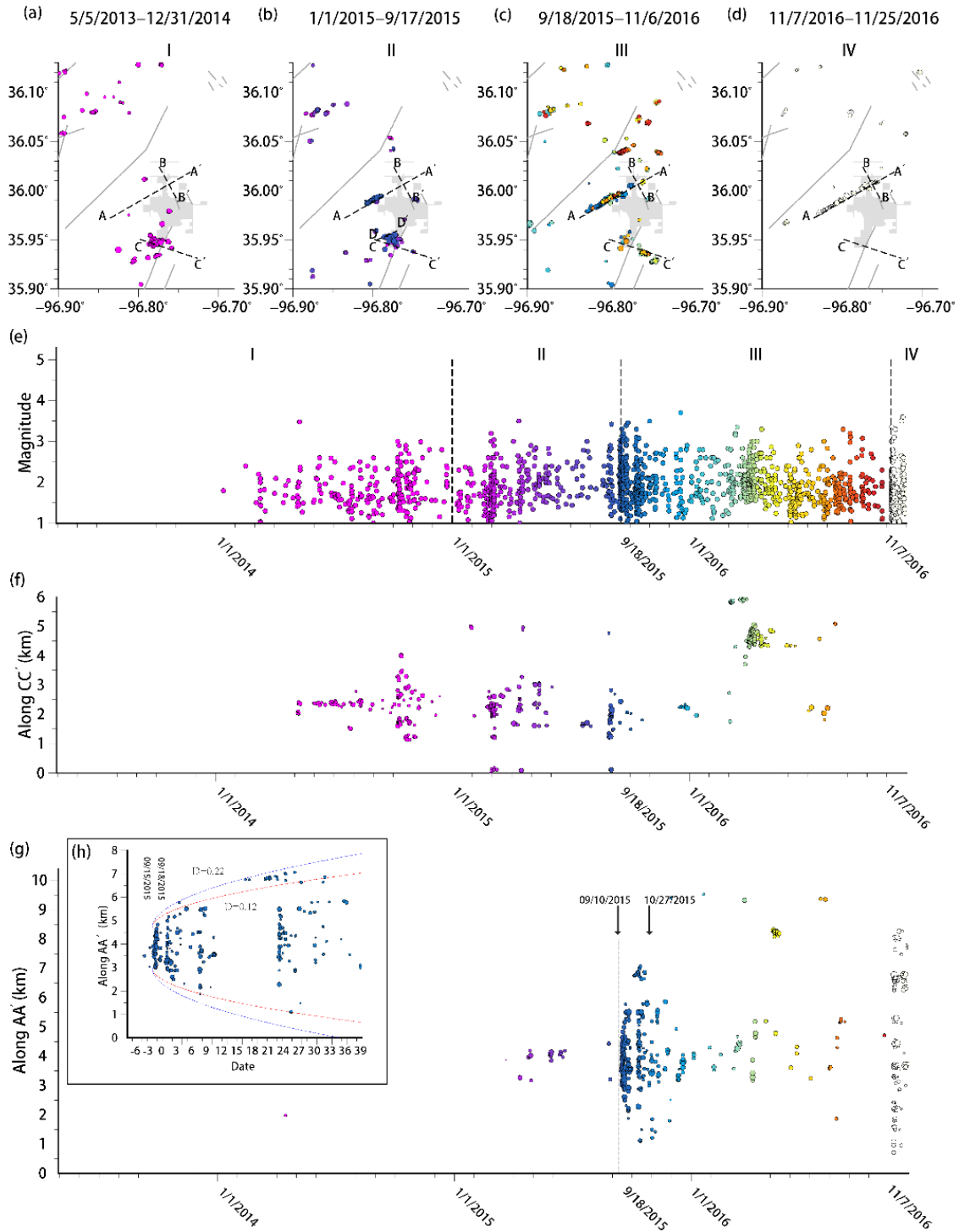


Figure S2. Geographic distribution of seismicity (Skoumal et al., 2019) for different time stages (a) I: May 2013 to Dec. 31, 2014. (b) II: Jan.1, 2015 to Sep.17, 2015 (c) III: Sep.18, 2015 to Nov. 6, 2016 (d) IV: Nov.7, 2016 to Dec.31, 2016. Fault AA' and DD' are right lateral and fault CC' is left lateral. (e) Magnitude-

Time plot of seismicity during each time stage I, II, III and IV. (f) Evolution of the earthquake locations along fault CC' vs time. (g) Evolution of the earthquake locations along fault AA' vs time. (h) A zoomed-in plot showing earthquake evolution within the dashed box in (g). Two colored dashed lines show the fluid diffusion curves with diffusivity  $D=0.12$  (red) and  $D=0.22$  (blue).

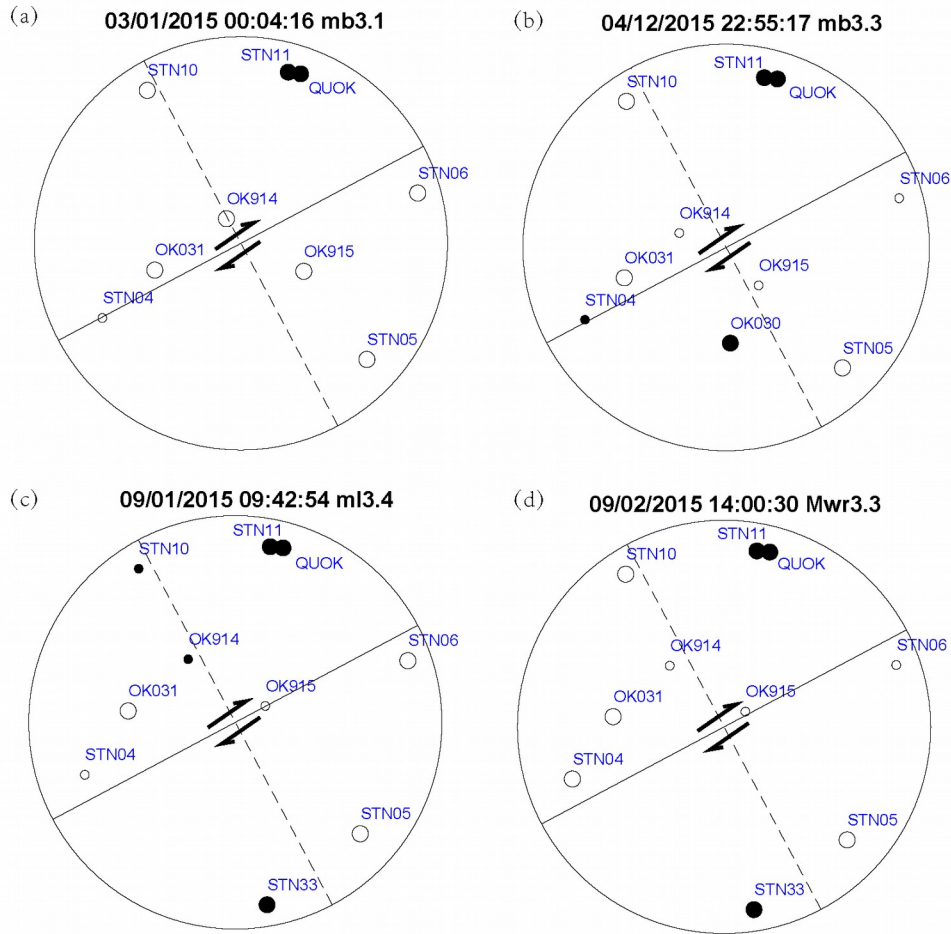


Figure S3. The P wave first motions for four  $M > 3$  earthquakes (a-d) along DD' in Figure 2(b), with solid circles representing stations with positive first motion on vertical direction and hollow circles representing stations with negative first motion on vertical direction. The radiuses of the circles are roughly calculated based on the take-off angles of each station, using a half-space uniform velocity. The first motions of four events infer that these earthquakes are consistent with 62 degrees right-lateral strike-slip fault, shown by solid straight lines and arrows, similar to the AA' Cushing fault.

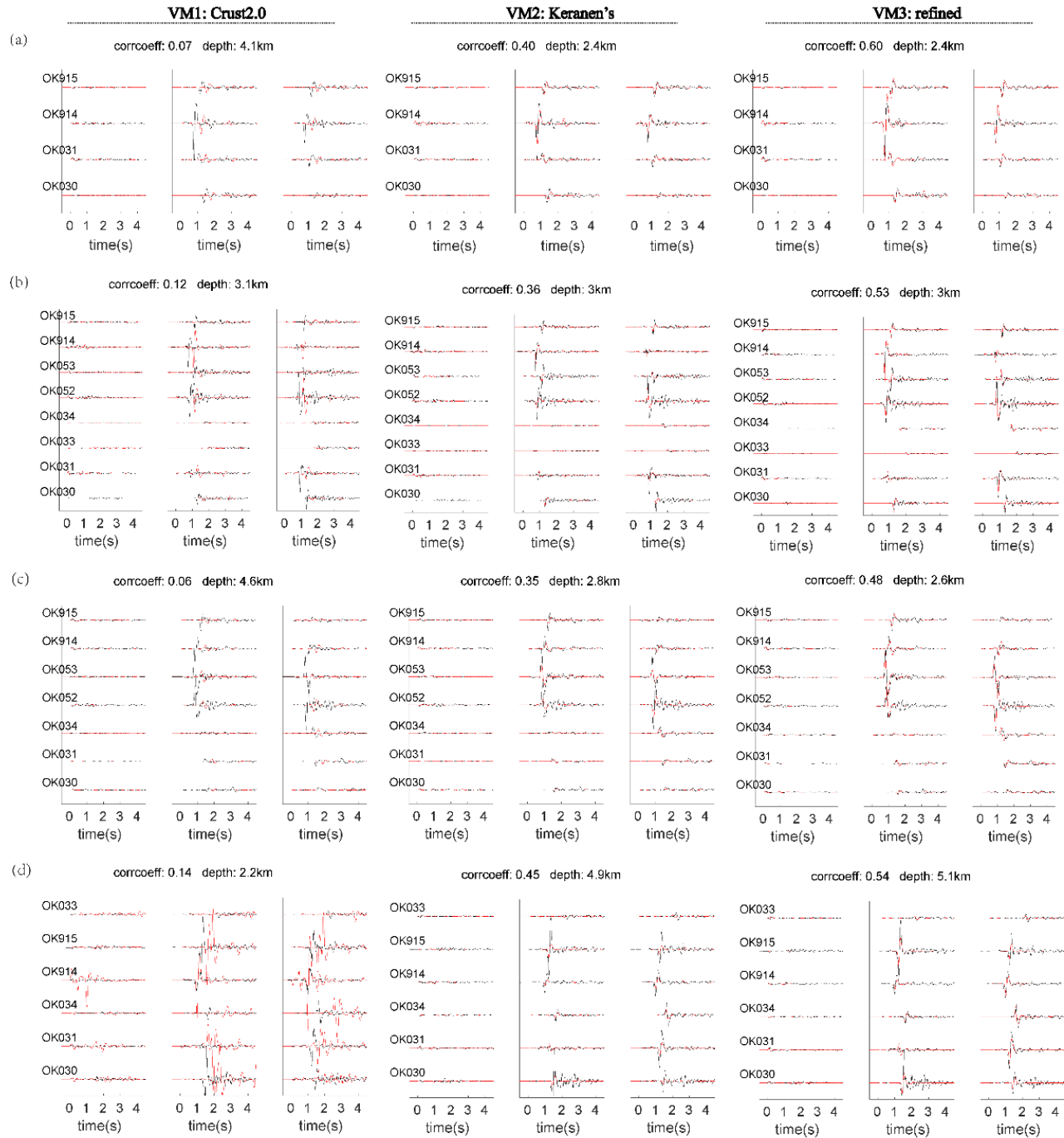


Figure S4. Waveform matches for four reference events (Table S1) under three velocity models in Figure 3. Left, central and right columns are for velocity models of VM1, VM2 and VM3 respectively. Observed and synthetic seismograms are displayed as black and red traces, respectively. (a) Reference event# 1 occurring on Nov 10, 2015 with Mw 3.3. (b) Reference event #2 occurring on Nov 11, 2016 with ML 3.1.

(c) Reference event #3 occurring on Nov. 22, 2016 with Mw 3.5. (d) Reference event #4 occurring on Nov. 24, 2016 with ML 3.6.

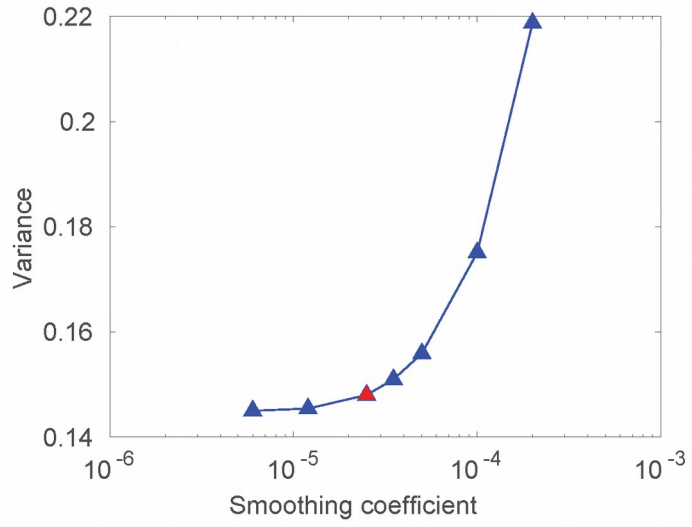


Figure S5. Waveform variance vs smoothing coefficient for the M 5 earthquake. Red triangle denotes the preferred value in this study:  $3.5 \times 10^{-5}$ .

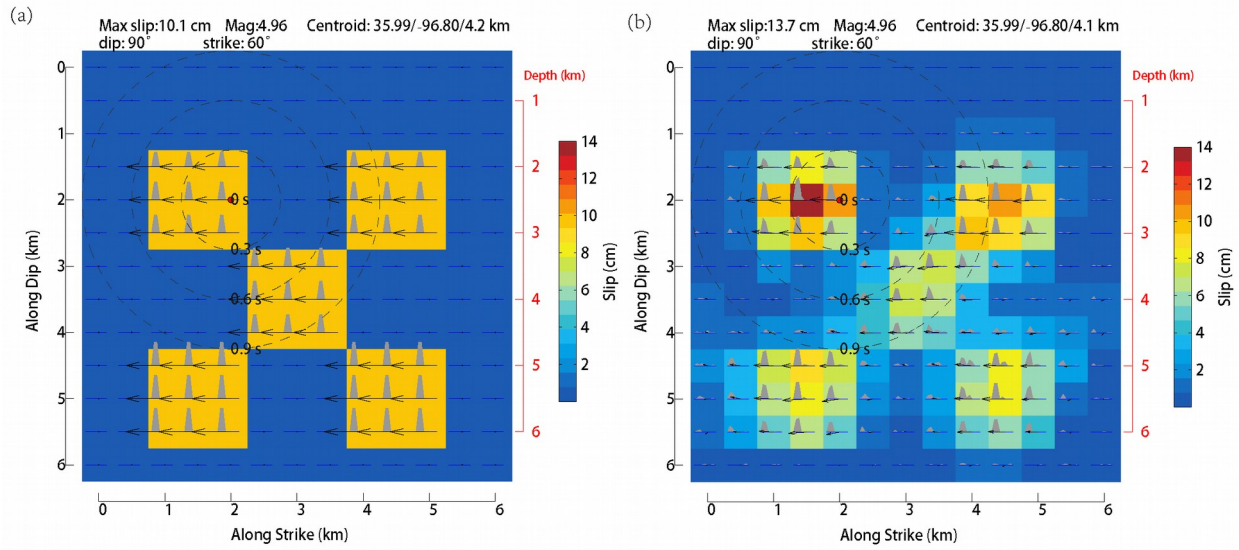


Figure S6. Check board tests for the finite fault inversion. (a) Input slip model. (b) Reconstructed slip model. The smoothing factor is  $3.5 \times 10^{-5}$ .

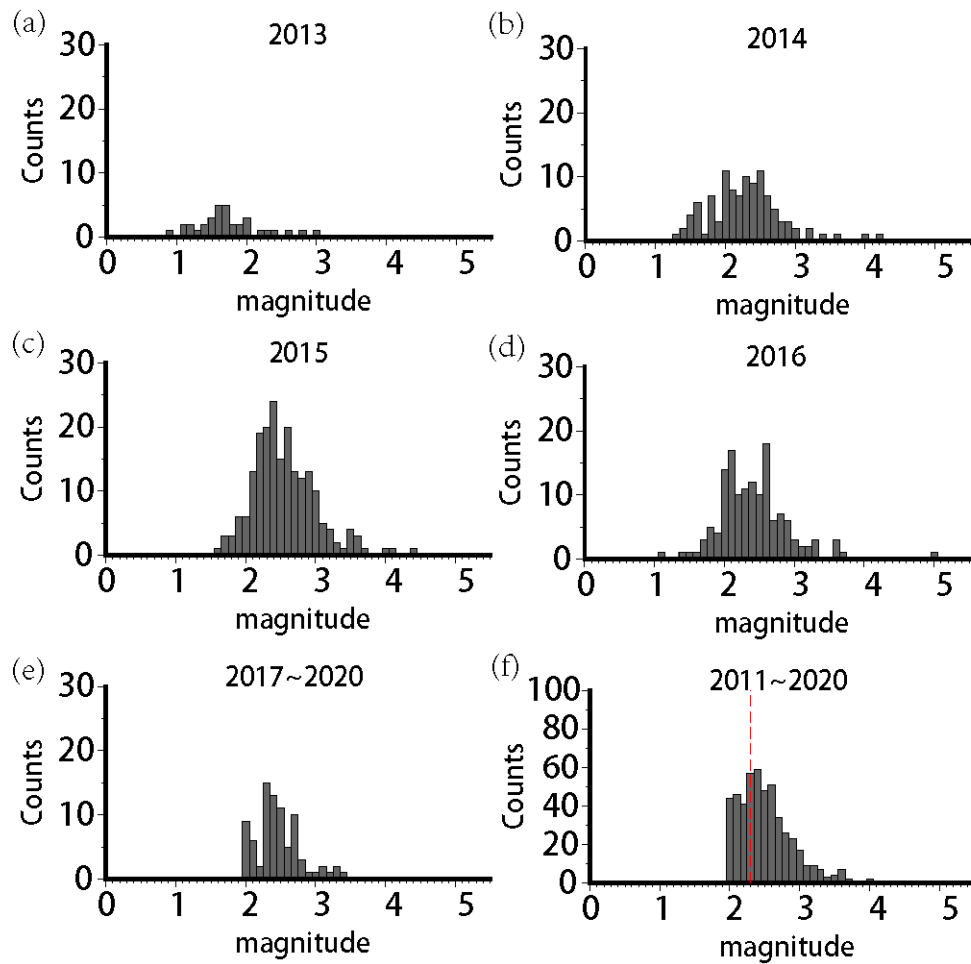


Figure S7. (a-e) Magnitude histograms of earthquakes in 2013,2014,2015,2016 and 2017-2020, within epicentral distance smaller than 10 miles from the hypocenters of Cushing earthquake sequence. (f)

Magnitude histogram of all earthquakes within epicentral distance of 10 miles, in year 2011 to 2020.

The earthquake catalog is from OGS and the preferred magnitude completeness is M 2.3, as shown in (f).

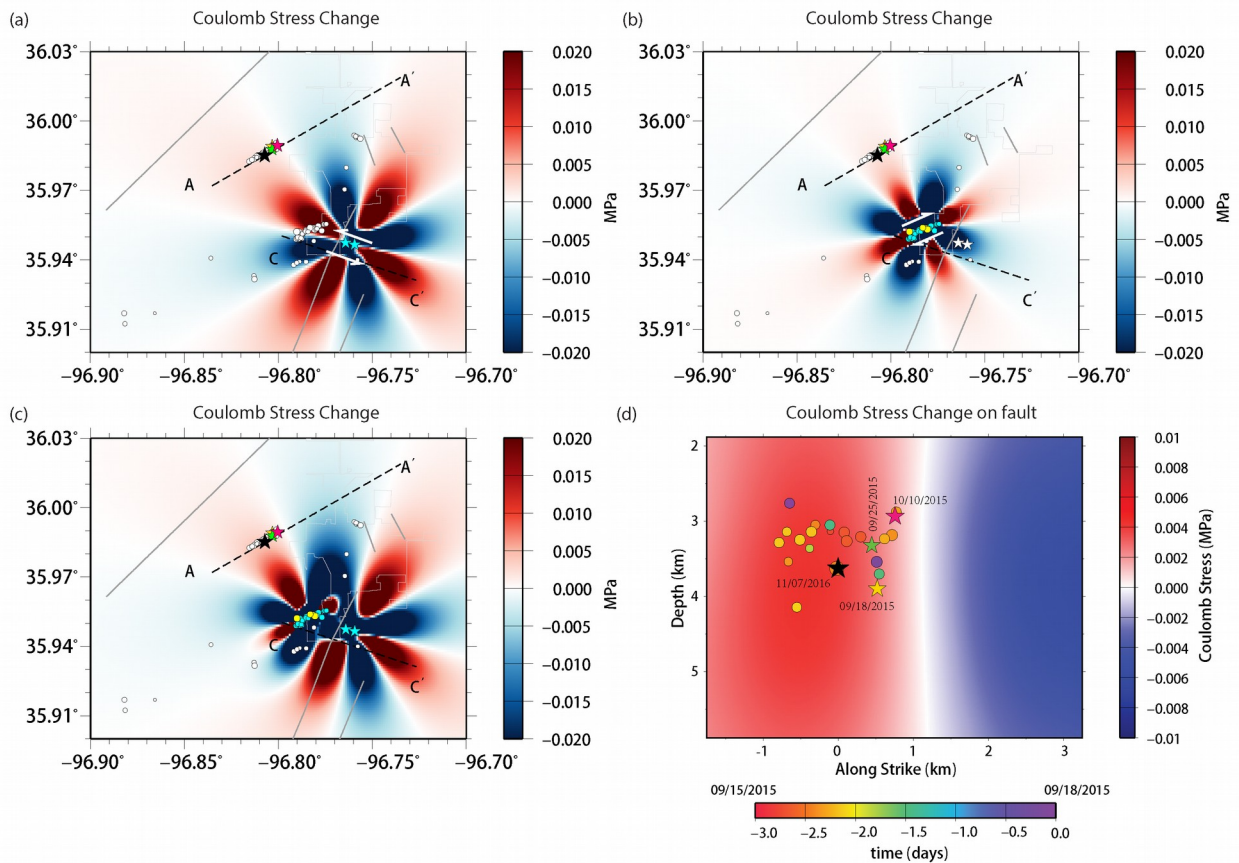


Figure S8. Coulomb stress changes resolved on right-lateral fault, striking 60 degrees with effective friction coefficient on fault set as 0.1 (a) Coulomb stress change at depth of 3 km, caused by two M4 left-lateral earthquakes (cyan stars) occurred in October 2014 on the south of Cushing city. (b) Coulomb stress change at depth of 3 km, caused by many right-lateral strike-slip earthquakes (cyan circles) occurred after two left-lateral M4 earthquakes in 2014 and before the Mw 4.1 09/18/2015 earthquake. The yellow circles are  $M > 3$  earthquakes shown in Figure S3. (c) Coulomb stress change at depth of 3 km, contributed from two left-lateral 2014 M4 earthquakes (cyan stars) and the right-lateral earthquakes (cyan circles) mentioned in (a) and (b). (d) Coulomb stress change on the cross section along AA' Cushing fault, caused by the left-lateral and right-lateral earthquake mentioned in (a)-(c). The colored circles are foreshocks occurred within three days before the 09/18/2015 Mw 4.1 event, with color of

circles representing relative earthquake occurrence time. The locations of Cushing earthquake sequence in this study are marked by colored stars and label by time.

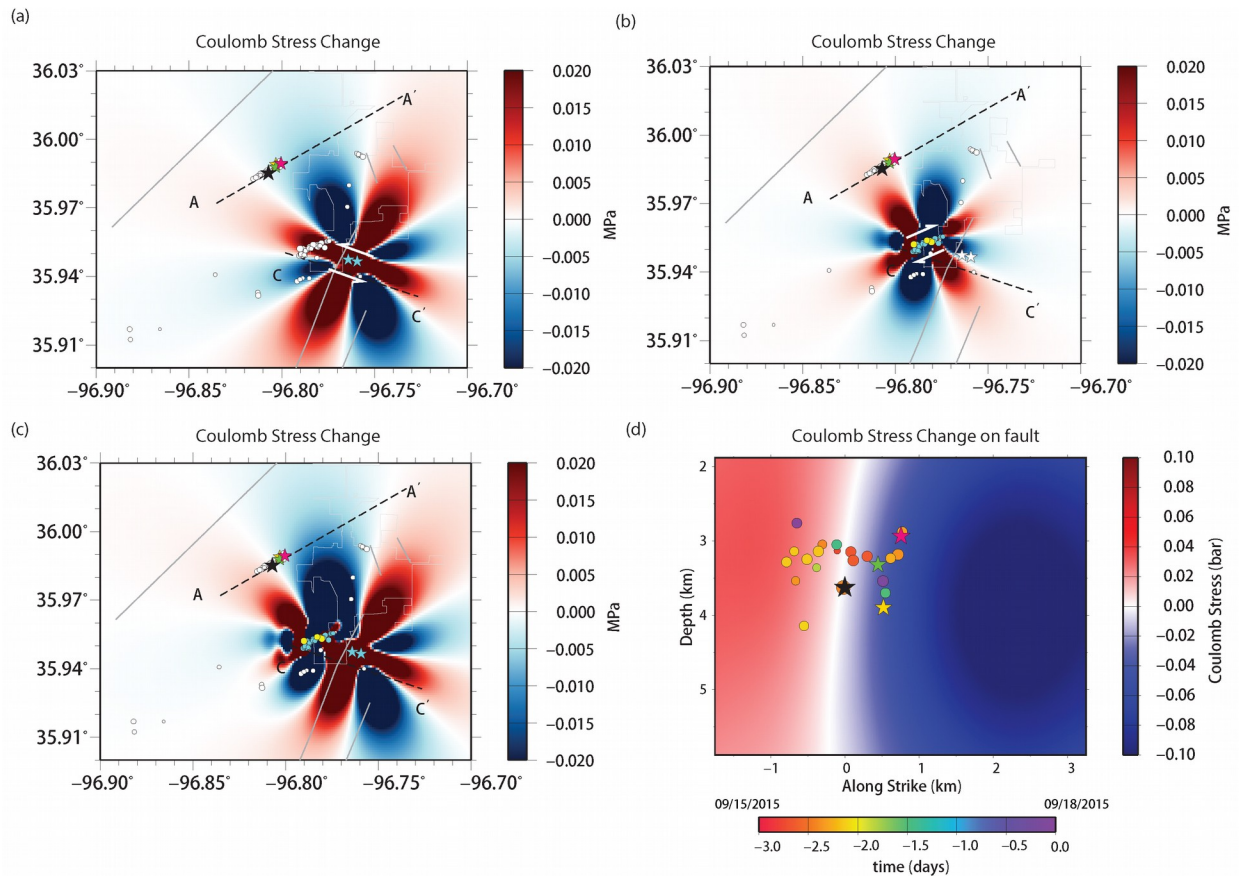


Figure S9. Coulomb stress changes resolved on right-lateral fault, striking 60 degrees with effective friction coefficient on fault set as 0.68 (a) Coulomb stress change at depth of 3 km, caused by two M4 left-lateral earthquakes (cyan stars) occurred in October 2014 on the south of Cushing city. (b) Coulomb stress change at depth of 3 km, caused by many right-lateral strike-slip earthquakes (cyan circles) occurred after two left-lateral M4 earthquakes in 2014 and before the Mw 4.1 09/18/2015 earthquake. The yellow circles are  $M > 3$  earthquakes shown in Figure S3. (c) Coulomb stress change at depth of 3 km, contributed from two left-lateral 2014 M4 earthquakes (cyan stars) and the right-lateral earthquakes (cyan circles) mentioned in (a) and (b). (d) Coulomb stress change on the depth section along AA' Cushing fault, caused by the left-lateral and right-lateral earthquake mentioned in (a)-(c). The colored circles are foreshocks occurred within three days before the 09/18/2015 Mw 4.1 event, with color of

circles representing relative earthquake occurrence time. The locations of Cushing earthquake sequence in this study are marked by colored stars and label by time.